ATLAS NOTE

ATLAS-CONF-2012-033

March 11, 2012

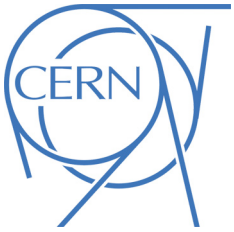

Search for squarks and gluinos with the ATLAS detector using final states with jets and missing transverse momentum and 4.7 fb^{-1} of $\sqrt{s}$ = 7 TeV proton-proton collision data

ATLAS Collaboration

Abstract

A search for squarks and gluinos in final states containing jets, missing transverse momentum and no high-p_{T} electrons or muons is presented. The data represent the complete sample recorded in 2011 by the ATLAS experiment in $\sqrt{s}$ = 7 TeV proton-proton collisions at the Large Hadron Collider, with a total integrated luminosity of 4.7 fb^{-1}. No excess above the Standard Model background expectation is observed. Gluino masses below 940 GeV, and squark masses below 1380 GeV are excluded at the 95% confidence level in simplified models containing only squarks of the first two generations, a gluino octet and a massless neutralino. In MSUGRA/CMSSM models with $\tan\beta = 10$, $A_0 = 0$ and $\mu > 0$, squarks and gluinos of equal mass are excluded for masses below 1400 GeV. These limits considerably extend the region of supersymmetric parameter space excluded by previous measurements with the ATLAS detector.

1 Introduction

Many extensions of the Standard Model (SM) include heavy coloured particles, some of which could be accessible at the Large Hadron Collider (LHC) [1]. The squarks and gluinos of supersymmetric (SUSY) theories [2–10] form one class of such particles. This letter presents a new ATLAS search for squarks and gluinos in final states containing only jets and large missing transverse momentum. Interest in this final state is motivated by the large number of R-parity conserving models [11–15] in which squarks, $\tilde{q}$, and gluinos, $\tilde{g}$, can be produced in pairs $\{\tilde{g}\tilde{g}, \tilde{q}\tilde{q}, \tilde{q}\tilde{g}\}$ and can generate that final state in their decays $\tilde{q} \rightarrow q\tilde{\chi}_1^0$ and $\tilde{g} \rightarrow q\bar{q}\tilde{\chi}_1^0$ to weakly interacting neutralinos, $\tilde{\chi}_1^0$, which escape the detector unseen. The analysis presented here is based on a study of purely hadronic final states; events with reconstructed electrons or muons are vetoed to avoid overlap with a related ATLAS search [16] which requires them. Compared to to previous studies [17], this updated analysis uses the full dataset recorded in 2011(4.7 fb^{-1}) and extends the sensitivity of the search by selecting final state topologies with higher jet multiplicities. The search strategy was optimised for maximum discovery reach in the $(m_{\tilde{g}}, m_{\tilde{q}})$-plane (where $m_{\tilde{g}}, m_{\tilde{q}}$ are the gluino and squark masses respectively) for a range of models, including a simplified one in which all other supersymmetric particles, except for the lightest neutralino, were given masses beyond the reach of the LHC. Although interpreted in terms of SUSY models, the main results of this analysis (the data and expected background event counts in the signal regions) are relevant for constraining any model of new physics that predicts production of jets in association with missing transverse momentum.

2 The ATLAS Detector and Data Samples

The ATLAS detector [18] is a multipurpose particle physics apparatus with a forward-backward symmetric cylindrical geometry and nearly 4π coverage in solid angle.[1] The layout of the detector features four superconducting magnet systems, which comprise a thin solenoid surrounding inner tracking detectors and three large toroids supporting a large muon spectrometer. The calorimeters are of particular importance to this analysis. In the pseudorapidity region $|\eta| < 3.2$, high-granularity liquid-argon (LAr) electromagnetic (EM) sampling calorimeters are used. An iron-scintillator tile calorimeter provides hadronic coverage over $|\eta| < 1.7$. The end-cap and forward regions, spanning $1.5 < |\eta| < 4.9$, are instrumented with LAr calorimetry for both EM and hadronic measurements.

The data sample used in this analysis was taken in 2011 with the LHC operating at a centre-of-mass energy of 7 TeV. Application of beam, detector and data-quality requirements resulted in a total integrated luminosity of 4.7 fb^{-1}. The trigger required events to contain a leading jet with a transverse momentum (p_{T}), measured at the electromagnetic scale, above 75 GeV and missing transverse momentum above 55 GeV. The detailed trigger specification varied throughout the data-taking period, partly as a consequence of the rapidly increasing LHC luminosity. The trigger reached its full efficiency of > 98% for events with a reconstructed jet with p_{T} exceeding 130 GeV and more than 160 GeV of missing transverse momentum.

3 Object Reconstruction

Jet candidates are reconstructed using the anti-k_t jet clustering algorithm [19, 20] with a distance parameter of 0.4. The inputs to this algorithm are clusters [21] of calorimeter cells seeded by those with energy significantly above the measured noise. Jet momenta are constructed by performing a four-vector

[1] ATLAS uses a right-handed coordinate system with its origin at the nominal interaction point in the centre of the detector and the z-axis along the beam pipe. Cylindrical coordinates (r, ϕ) are used in the transverse plane, ϕ being the azimuthal angle around the beam pipe. The pseudorapidity η is defined in terms of the polar angle θ by $\eta = -\ln\tan(\theta/2)$.

sum over these cell clusters, measured at the electromagnetic scale, treating each as an $(E, \vec{p})$ four-vector with zero mass. The jet energies are corrected for the effects of calorimeter non-compensation and inhomogeneities by using p_{T}- and η-dependent calibration factors based on Monte Carlo (MC) corrections validated with extensive test-beam and collision-data studies [22]. Only jet candidates with $p_{\mathrm{T}} > 20$ GeV are subsequently retained.

Electron candidates are required to have $p_{\mathrm{T}} > 20$ GeV and $|\eta| < 2.47$, and to pass the 'medium' electron shower shape and track selection criteria described in Ref. [23]. Muon candidates are required to have $p_{\mathrm{T}} > 10$ GeV and $|\eta| < 2.4$.

Following the steps above, overlaps between candidate jets with $|\eta| < 2.8$ and leptons are resolved as follows [24]. First, any such jet candidate lying within a distance $\Delta R = \sqrt{\Delta\eta^2 + \Delta\phi^2} < 0.2$ of an electron is discarded; then any lepton candidate remaining within a distance $\Delta R = 0.4$ of any surviving jet candidate is discarded.

The measurement of the missing transverse momentum two-vector $\vec{P}_{\mathrm{T}}^{\,\mathrm{miss}}$ (and its magnitude $E_{\mathrm{T}}^{\mathrm{miss}}$) is based on the transverse momenta of all remaining jet and lepton candidates and all calorimeter clusters not associated to such objects. Following this step, all jet candidates with $|\eta| > 2.8$ are discarded. Thereafter, the remaining lepton and jet candidates are considered "reconstructed", and the term "candidate" is dropped.

4 Signal and Control Region Definitions

Following the object reconstruction described above, events are discarded if any electrons with $p_{\mathrm{T}} > 20$ GeV or muons with $p_{\mathrm{T}} > 10$ GeV remain, or if they have any jets failing quality selection criteria designed to suppress detector noise and non-collision backgrounds (see e.g. Ref. [25]), or if they lack a reconstructed primary vertex associated with five or more tracks.

This analysis aims to search for the production of heavy SUSY particles decaying into jets and neutralinos, with the latter creating missing transverse momentum ($E_{\mathrm{T}}^{\mathrm{miss}}$). Because of the high mass scale expected for the SUSY signal, the 'effective mass', m_{eff}, is a powerful discriminant between the signal and most Standard Model backgrounds. For a channel which selects events with N jets, m_{eff} is defined to be the scalar sum of the transverse momenta of the leading N jets together with $E_{\mathrm{T}}^{\mathrm{miss}}$. The final signal selection uses cuts on m_{eff}(incl.) which sums over all jets with $p_{\mathrm{T}} > 40$ GeV. Cuts on m_{eff} and $E_{\mathrm{T}}^{\mathrm{miss}}$, which suppress the multi-jet background, formed the basis of the previous ATLAS jets+ $E_{\mathrm{T}}^{\mathrm{miss}}$ + 0-lepton SUSY search [26]. The same strategy is adopted in this analysis.

The requirements used to select jets and leptons (which are referred to as physics objects) are chosen to give sensitivity to a broad range of SUSY models. In order to achieve maximal reach over the $(m_{\tilde{g}}, m_{\tilde{q}})$-plane, six analysis channels are defined. Squarks typically generate at least one jet in their decays, for instance through $\tilde{q} \to q\tilde{\chi}_1^0$, while gluinos typically generate at least two, for instance through $\tilde{g} \to q\bar{q}\tilde{\chi}_1^0$. Processes contributing to $\tilde{q}\tilde{q}$, $\tilde{q}\tilde{g}$ and $\tilde{g}\tilde{g}$ final states therefore lead to events containing at least two, three or four jets, respectively. Cascade decays of heavy particles tend to further increase the final state multiplicity.

Five inclusive analysis channels, labelled A to E and characterized by increasing jet multiplicity from 2 to 6, are therefore defined. In addition, the two jet sample is divided into two channels, A and A', using the ratio of the $E_{\mathrm{T}}^{\mathrm{miss}}$ to the m_{eff}. Channel A' is designed to improve the sensitivity to models with small sparticle mass splittings, where the presence of initial state radiation jets may allow signal events to be selected irrespective of the visibility of the sparticle decay products. The lower jet multiplicity channels focus on models characterised by squark pair production with short decay chains, while those requiring high jet multiplicity are optimised for gluino pair production and/or long cascade decay chains. The channels and signal regions (SRs) are summarised in Table 1.

Requirement	Channel					
	A	A'	B	C	D	E
$E_{\mathrm{T}}^{\mathrm{miss}}$[GeV] >	160					
$p_{\mathrm{T}}(j_1)$ [GeV] >	130					
$p_{\mathrm{T}}(j_2)$ [GeV] >	60					
$p_{\mathrm{T}}(j_3)$ [GeV] >	–	–	60	60	60	60
$p_{\mathrm{T}}(j_4)$ [GeV] >	–	–	–	60	60	60
$p_{\mathrm{T}}(j_5)$ [GeV] >	–	–	–	–	40	40
$p_{\mathrm{T}}(j_6)$ [GeV] >	–	–	–	–	–	40
$\Delta\phi(\mathrm{jet}, E_{\mathrm{T}}^{\mathrm{miss}})_{\mathrm{min}}$ >	0.4 ($i = \{1, 2, (3)\}$)			0.4 ($i = \{1, 2, 3\}$), 0.2 ($p_{\mathrm{T}} > 40$ GeV jets)		
$E_{\mathrm{T}}^{\mathrm{miss}}/m_{\mathrm{eff}}(Nj)$ >	0.3 (2j)	0.4 (2j)	0.25 (3j)	0.25 (4j)	0.2 (5j)	0.15 (6j)
m_{eff}(incl.) [GeV] >	1900/1400/–	–/1200/–	1900/–/–	1500/1200/900	1500/–/–	1400/1200/900

Table 1: Cuts used to define each of the channels in the analysis. The $E_{\mathrm{T}}^{\mathrm{miss}}/m_{\mathrm{eff}}$ cut in any N jet channel uses a value of m_{eff} constructed from only the leading N jets (indicated in parentheses). However, the final m_{eff}(incl.) selection, which is used to define the signal regions, includes all jets with $p_{\mathrm{T}} > 40$ GeV. The three m_{eff}(incl.) selections listed in the final row denote the 'tight', 'medium' and 'loose' selections respectively. Not all channels include all three SRs.

In Table 1, $\Delta\phi(\mathrm{jet}, E_{\mathrm{T}}^{\mathrm{miss}})_{\mathrm{min}}$ is the smallest of the azimuthal separations between $\vec{P}_{\mathrm{T}}^{\,\mathrm{miss}}$ and the reconstructed jets. For channels A, A' and B, the selection requires $\Delta\phi(\mathrm{jet}, E_{\mathrm{T}}^{\mathrm{miss}})_{\mathrm{min}} > 0.4$ using up to three leading jets. For the other channels an additional requirement $\Delta\phi(\mathrm{jet}, E_{\mathrm{T}}^{\mathrm{miss}})_{\mathrm{min}} > 0.2$ is placed on all jets with $p_{\mathrm{T}} > 40$ GeV. Requirements on $\Delta\phi(\mathrm{jet}, E_{\mathrm{T}}^{\mathrm{miss}})_{\mathrm{min}}$ and $E_{\mathrm{T}}^{\mathrm{miss}}/m_{\mathrm{eff}}$ are designed to reduce the background from multi-jet processes.

Standard Model background processes contribute to the event counts in the signal regions. The dominant sources are: W+jets, Z+jets, top quark pair, single top quark, and multi-jet production, with a smaller contribution from diboson production. The majority of the W+jets background is composed of $W \to \tau\nu$ events, or $W \to e\nu, \mu\nu$ events in which no electron or muon candidate is reconstructed. The largest part of the Z+jets background comes from the irreducible component in which $Z \to \nu\bar{\nu}$ decays generate large $E_{\mathrm{T}}^{\mathrm{miss}}$. Top quark pair production followed by semileptonic decays, in particular $t\bar{t} \to b\bar{b}\tau\nu qq$ with the τ-lepton decaying hadronically, as well as single top quark events, can also generate large $E_{\mathrm{T}}^{\mathrm{miss}}$ and pass the jet and lepton requirements at a non-negligible rate. The multi-jet background in the signal regions is caused by misreconstruction of jet energies in the calorimeters leading to apparent missing transverse momentum, as well as by neutrino production in semileptonic decays of heavy quarks. Extensive validation of the MC simulation against data has been performed for each of these background sources and for a wide variety of control regions (CRs).

Each of the six channels is used to construct between one and three signal regions with 'tight', 'medium' and/or 'loose' m_{eff}(incl.) selections. In order to estimate the backgrounds in a consistent and robust fashion, five control regions are defined for each of the eleven signal regions, giving 55 CRs in total. The orthogonal CR event selections are designed to provide uncorrelated data samples enriched in particular background sources. Each ensemble of one SR and five CRs constitutes a different 'stream' of the analysis. The CR selections are optimised to maintain adequate statistical weight, while minimising as far as possible the systematic uncertainties arising from extrapolation to the SR.

The control regions are chosen to be as close kinematically as possible to the corresponding SR in order to minimise theoretical uncertainties arising from extrapolation between them. The CRs are listed

CR	SR Background	CR process	CR selection
CR1a	$Z(\to \nu\nu)$+jets	γ+jets	Isolated photon
CR1b	$Z(\to \nu\nu)$+jets	$Z(\to \ell\ell)$+jets	$\lvert m(\ell,\ell) - m(Z)\rvert < 25$ GeV
CR2	Multi-jets	Multi-jets	Reversed $\Delta\phi(j_i, E_{\mathrm{T}}^{\mathrm{miss}})$ cut
CR3	$W(\to \ell\nu)$+jets	$W(\to \ell\nu)$+jets	30 GeV $< m_T(\ell, E_{\mathrm{T}}^{\mathrm{miss}}) <$ 100 GeV, b-veto
CR4	$t\bar{t}$ and single-t	$t\bar{t} \to bbqq'\ell\nu$	30 GeV $< m_T(\ell, E_{\mathrm{T}}^{\mathrm{miss}}) <$ 100 GeV, b-tag

Table 2: Control regions used in the analysis: the main targeted background in the SR,, the process used to model the background, and main CR cut(s) used to select this process are given.

in Table 2. CR1a and CR1b are used to estimate the contribution of $Z(\to \nu\nu)$+jets background events to the SR by selecting samples of respectively γ+jets and $Z(\to \ell\ell)$+jets events. CR2 uses a reversed and tightened cut on the minimum angular separation in the transverse plane between up to three selected leading jets (depending on channel) and $\vec{P}_{\mathrm{T}}^{\,\mathrm{miss}}$ ($\Delta\phi(j_i, E_{\mathrm{T}}^{\mathrm{miss}})$ in Table 1) to produce a data sample enriched in multi-jet background events. CR3 and CR4 use respectively a b-jet veto or b-jet requirement together with a lepton+$E_{\mathrm{T}}^{\mathrm{miss}}$ transverse mass (m_{T}) requirement to select samples of $W(\to \ell\nu)$+jets and semi-leptonic $t\bar{t}$ background events. All other cuts are similar to those used to select the corresponding signal region.

The observed numbers of events in the CRs for each SR are used to generate internally consistent SM background estimates for the SR via a likelihood fit. This procedure enables CR correlations and contamination by other SM processes and/or SUSY signal events to be taken into account. The same fit also allows the statistical significance of the observation in the SR to be determined. Key ingredients in the fit are the ratios of expected event counts (the TFs) from each background process between the SR and each CR, and between CRs. The TFs enable observations in the CRs to be converted into background estimates in the SR using:

$$\mathrm{N(SR, est, proc)} = \mathrm{N(CR, obs, proc)} \times \left[\frac{\mathrm{N(SR, raw, proc)}}{\mathrm{N(CR, raw, proc)}}\right], \tag{1}$$

where N(SR, est, proc) is the estimated background contribution to the SR by a given process, N(CR, obs, proc) is the observed number of data events in the CR for the process, and N(SR, initial, proc) and N(CR, initial, proc) are initial, un-normalised estimates of the contributions from the process to the SR and CR, respectively. The ratio appearing in the square brackets in Eqn. 1 is defined to be the transfer factor TF. Similar equations containing inter-CR TFs enable the background estimates to be normalised coherently across all the CRs.

Background estimation requires determination of the central expected values of the TFs for each SM process, together with their associated correlated and uncorrelated uncertainties. The multi-jet TFs are estimated using a data-driven technique, which applies a resolution function to well-measured multi-jet events in order to estimate the effect on $E_{\mathrm{T}}^{\mathrm{miss}}$ and other variables. The other TFs estimates use fully simulated Monte Carlo samples validated with data. Some systematic uncertainties, for instance those arising from the jet energy scale (JES), or theoretical uncertainties in MC cross-sections, largely cancel when calculating the event count ratios constituting the TFs.

The result of the likelihood fit for each SR-CR ensemble is a set of background estimates and uncertainties for the SR together with a p-value giving the probability for the hypothesis that the SR event count is compatible with background alone. However, an assumption has to be made about the migration of SUSY signal events between regions. When searching for a SUSY signal in a particular SR, it is assumed that the signal contributes only to the SR, i.e. the SUSY TFs are all set to zero, giving no contribution from the signal in the CRs. If no excess is observed, then limits are set within specific

SUSY parameter spaces, taking into account theoretical and experimental uncertainties on the SUSY production cross-section and kinematic distributions. Exclusion limits are obtained using a likelihood test. This compares the observed event rates in the signal regions with the fitted background expectation and expected signal contributions, for various signal hypotheses.

MC simulation samples are used to develop the analysis, optimise the selections, determine the transfer factors used to estimate the W+jets, Z+jets and top quark production backgrounds, and to assess sensitivity to specific SUSY signal models. Samples of simulated QCD jet events are generated with PYTHIA [27], using the MRST2007LO* modified leading-order parton distribution functions (PDFs) [28]. Production of top quark pairs is simulated with ALPGEN [29] and PDF set CTEQ6L1 [30] (with a top quark mass of 172.5 GeV). Samples of W and Z/γ^* events with accompanying jets are also produced with ALPGEN. Diboson (WW, WZ, ZZ, $W\gamma^*$) production is simulated with SHERPA [31]. Single top production is simulated with MC@NLO [32,33], and the Next-to-Leading Order (NLO) PDF set CTEQ6.6 [34], which is used for all NLO MC. Drell-Yan is simulated with PYTHIA. Fragmentation and hadronization for the ALPGEN and MC@NLO samples is performed with HERWIG [35, 36], using JIMMY [37] for the underlying event. For the γ+jet estimates of the $Z(\rightarrow \nu\nu)$+jet backgrounds, photon and Z events are both produced using SHERPA for consistency.

Supersymmetric events are generated with HERWIG++ [38], normalised using NLO cross sections. These include the Next-to-Leading Order supersymmetric QCD corrections and the resummation of soft gluon emission at Next-to-Leading-Logarithmic accuracy, calculated with NLL-fast [39–43] for $m_{\tilde{g}} < 2$ TeV and $m_{\tilde{q}} < 4.5$ TeV. When NLL-fast cross-sections are unavailable, (e.g. for electroweak and associated strong and electroweak processes), PROSPINO [39] is used instead. The central values of the cross-sections are obtained following the PDF4LHC [44] recommendations (using only the CTEQ6.6 and MSTW2008 [45] PDF sets).

The MC samples are generated using the ATLAS MC11 production parameter set [46–48] and a GEANT4 [49] based detector simulation [50]. Differing pile-up (multiple proton-proton interactions in a given bunch-crossing) conditions as a function of the LHC instantaneous luminosity are taken into account by overlaying minimum-bias events to the hard-scattering process and reweighting them according to the mean number of interactions expected.

5 Systematic Uncertainties

Systematic uncertainties arise through the use of the transfer factors relating observations in the control regions to background expectations in the signal regions, and from the modelling of the SUSY signal. For the MC-derived transfer factors the primary common sources of systematic uncertainty are the jet energy scale calibration, jet energy resolution (JER), MC modelling and the reconstruction performance in the presence of pile-up.

The JES uncertainty has been measured from the complete 2010 data set using the techniques described in Ref. [22] and is around 4%, with a slight dependence upon p_{T}, η and proximity to adjacent jets,. The JER uncertainty was estimated using the methods discussed in [22]. Additional contributions are added to both the JES and the JER uncertainties to take account of the effect of pile-up at the relatively high luminosity delivered by the LHC in the 2011 run. Both in-time pile-up, multiple collisions within the same bunch-crossing, and out-of-time pile-up, which arises from the detector response to neighbouring bunch crossings, are accounted for.

The dominant modelling uncertainty in the MC estimate of the number of events in the signal and control regions arises from the impact of jet radiation on m_{eff}. In order to assess this uncertainty, alternative samples were produced with reduced initial parton multiplicities (ALPGEN processes with 0–5 partons rather than 0–6 partons for W/Z+jets production, and 0-3 instead of 0-5 for top pairs).

Additional uncertainties arising from photon and lepton reconstruction efficiency, energy scale and

resolution in CR1, CR3 and CR4, b-tag/veto efficiency (CR3 and CR4) and photon acceptance and cosmic ray backgrounds (CR1) are also considered. Uncertainties on the multi-jet transfer factors are dominated by the modelling of the p_{T} dependence of the Gaussian part of the response function. Other sources, including the limited MC event statistics as well as additional systematic uncertainties related to the response function, are also considered.

Systematic uncertainties on the expected SUSY signal were estimated through variations of the factorisation and renormalisation scales between half and twice their default values and by considering the PDF uncertainties following the PDF4LHC [44] recommendations. Uncertainties were calculated for individual production processes (e.g. $\tilde{q}\tilde{q}$, $\tilde{g}\tilde{g}$, etc.).

6 Results, Interpretation and Limits

The number of events observed in the data and the number of SM events expected to enter each of the signal regions, determined using the likelihood fit, are shown in Table 3. Good agreement is observed between the data and the SM prediction, with no significant excess.

Distributions of m_{eff} (prior to the final m_{eff} cuts) for each channel for data and normalised MC samples are shown in Figures 1–6. Equivalent distributions for the CRs can be found in Appendix A. For illustrative purposes, the ALPGEN W+jets, Z+jets and $t\bar{t}$+jets distributions in all cases are scaled by factors of respectively 0.75, 0.78 and 0.73 with respect to the normalisation by cross-section times luminosity, in order to improve the agreement with the data. These scaling factors are within the expected range of systematic uncertainties and are determined by normalisation to all data (i.e. without any m_{eff} cut) in CR3, CR1b and CR4 respectively in channel A (i.e. two-jet events). The CR1a plots use ALPGEN without any scaling.

Data from all the channels are used to set limits on SUSY models, taking the channel with the best expected sensitivity at each point in parameter space, up to maximum squark and gluino masses of 2 TeV. The $\mathrm{CL_s}$ prescription [51] is used to derive 95% Confidence Level (CL) exclusion regions. The result for each channel is obtained from the simultaneous fit to the signal region and each of the control regions. The use of transfer factors between all of these regions allows systematic uncertainties and nuisance parameters to be dealt with in a coherent way, preserving any correlations, as described above.

An interpretation of the results is presented in Figure 7 as a 95% CL exclusion region in the $(m_{\tilde{g}}, m_{\tilde{q}})$-plane for a simplified set of SUSY models with $m_{\tilde{\chi}_1^0} = 0$. In these models the gluino mass and the masses of the squarks of the first two generations are set to the values shown in the figure. All other supersymmetric particles, including the squarks of the third generation, are decoupled by being given masses of 5 TeV. ISASUSY from ISAJET [52] v7.80 is used to calculate the decay tables, and to guarantee consistent electroweak symmetry breaking. The results are also interpreted in the $\tan\beta = 10$, $A_0 = 0$, $\mu > 0$ slice of MSUGRA/CMSSM models[2] [53–58] in Figure 7. Additional figures in Appendix B show which signal regions contribute to the exclusion across the parameter spaces.

In the simplified model with light neutralinos, with the assumption that the coloured sparticles are directly produced and decay directly to jets and $E_{\mathrm{T}}^{\mathrm{miss}}$, the limit on the gluino mass is approximately 940 GeV, and on the squark mass is 1380 GeV. In the CMSSM/MSUGRA case, the limit on $m_{1/2}$ is above 300 GeV at high m_0 and reaches 680 GeV for low values of m_0. The inclusion of signal selections sensitive to larger jet multiplicities has improved significantly the ATLAS reach at large m_0. Equal mass squarks and gluinos are excluded below 1400 GeV in both scenarios.

[2]Five parameters are needed to specify a particular MSUGRA/CMSSM model: the universal scalar mass, m_0, the universal gaugino mass $m_{1/2}$, the universal trilinear scalar coupling, A_0, the ratio of the vacuum expectation values of the two Higgs fields, $\tan\beta$, and the sign of the higgsino mass parameter, $\mu = \pm$.

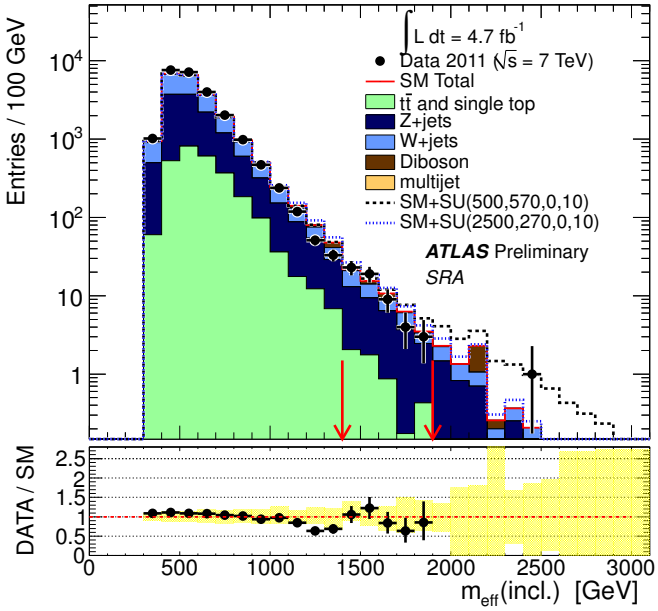

Figure 1: Observed m_{eff}(incl.) distribution for channel A. The histograms show the SM background expectations from MC. The ALPGEN W+jets, Z+jets and $t\bar{t}$ and single top distributions are normalised to data in corresponding control regions for channel A. The multi-jet background is estimated using a data-driven method, while the diboson contribution is normalised to luminosity. The yellow band shows only the combined JES, JER and MC statistics uncertainties. Other correlated systematic uncertainties, such as those due to theoretical modelling, are not shown. Two mSUGRA/CMSSM benchmark model points with m_0=500 GeV, $m_{1/2}$=570 GeV, A_0=0, $\tan\beta$=10 and $\mu > 0$ and with m_0=2500 GeV, $m_{1/2}$=270 GeV, A_0=0, $\tan\beta$=10 and $\mu > 0$, illustrating different topologies, are also shown. These points lie just beyond the reach of the previous analysis [17]. The red arrows indicate the locations of the lower edges of the two signal regions.

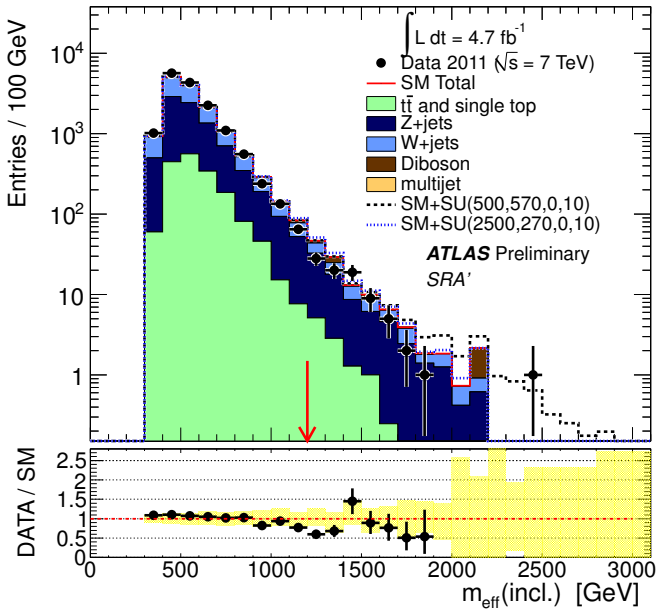

Figure 2: Observed m_{eff}(incl.) distribution for channel A'. The histograms show the SM background expectations from MC. The ALPGEN W+jets, Z+jets and $t\bar{t}$ and single top distributions are normalised to data in corresponding control regions for channel A. The multi-jet background is estimated using a data-driven method, while the diboson contribution is normalised to luminosity. The yellow band shows only the combined JES, JER and MC statistics uncertainties. Other correlated systematic uncertainties, such as those due to theoretical modelling, are not shown. Two mSUGRA/CMSSM benchmark model points with m_0=500 GeV, $m_{1/2}$=570 GeV, A_0=0, $\tan\beta$=10 and $\mu > 0$ and with m_0=2500 GeV, $m_{1/2}$=270 GeV, A_0=0, $\tan\beta$=10 and $\mu > 0$, illustrating different topologies, are also shown. These points lie just beyond the reach of the previous analysis [17]. The red arrow indicates the location of the lower edge of the signal region.

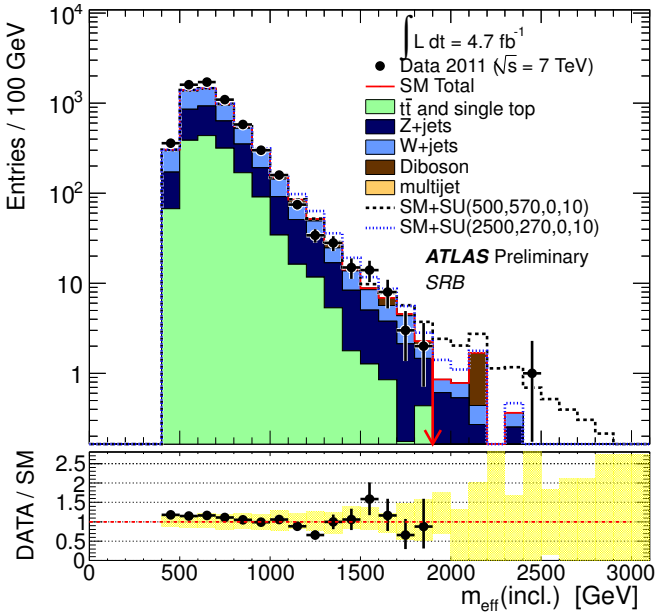

Figure 3: Observed m_{eff}(incl.) distribution for channel B. The histograms show the SM background expectations from MC. The ALPGEN W+jets, Z+jets and $t\bar{t}$ and single top distributions are normalised to data in corresponding control regions for channel A. The multi-jet background is estimated using a data-driven method, while the diboson contribution is normalised to luminosity. The yellow band shows only the combined JES, JER and MC statistics uncertainties. Other correlated systematic uncertainties, such as those due to theoretical modelling, are not shown. Two mSUGRA/CMSSM benchmark model points with m_0=500 GeV, $m_{1/2}$=570 GeV, A_0=0, $\tan\beta$=10 and $\mu > 0$ and with m_0=2500 GeV, $m_{1/2}$=270 GeV, A_0=0, $\tan\beta$=10 and $\mu > 0$, illustrating different topologies, are also shown. These points lie just beyond the reach of the previous analysis [17]. The red arrow indicates the location of the lower edge of the signal region.

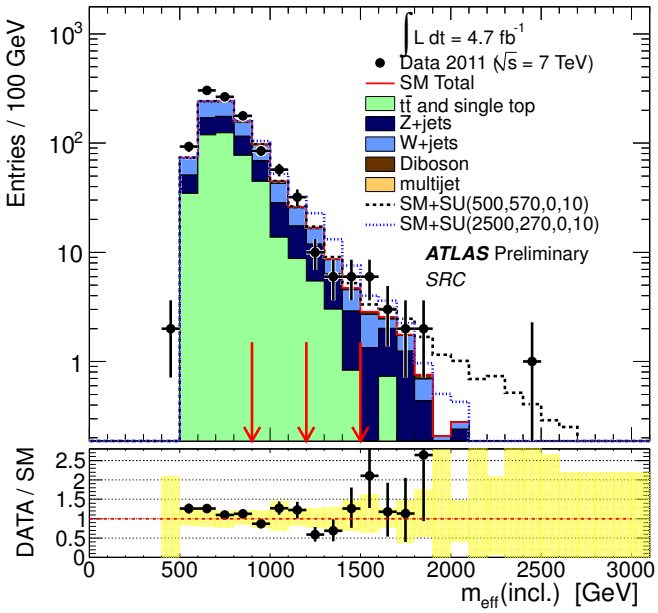

Figure 4: Observed m_{eff}(incl.) distribution for channel C. The histograms show the SM background expectations from MC. The ALPGEN W+jets, Z+jets and $t\bar{t}$ and single top distributions are normalised to data in corresponding control regions for channel A. The multi-jet background is estimated using a data-driven method, while the diboson contribution is normalised to luminosity. The yellow band shows only the combined JES, JER and MC statistics uncertainties. Other correlated systematic uncertainties, such as those due to theoretical modelling, are not shown. Two mSUGRA/CMSSM benchmark model points with m_0=500 GeV, $m_{1/2}$=570 GeV, A_0=0, $\tan\beta$=10 and $\mu > 0$ and with m_0=2500 GeV, $m_{1/2}$=270 GeV, A_0=0, $\tan\beta$=10 and $\mu > 0$, illustrating different topologies, are also shown. These points lie just beyond the reach of the previous analysis [17]. The red arrows indicate the locations of the lower edges of the three signal regions.

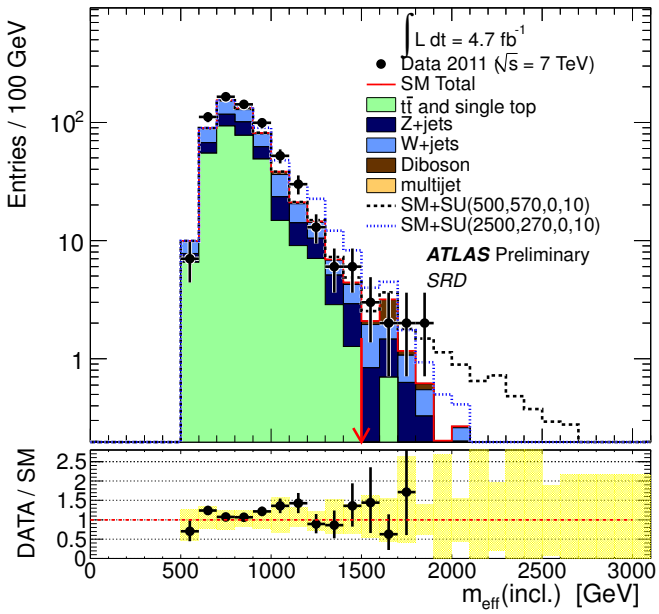

Figure 5: Observed m_{eff}(incl.) distribution for channel D. The histograms show the SM background expectations from MC. The ALPGEN W+jets, Z+jets and $t\bar{t}$ and single top distributions are normalised to data in corresponding control regions for channel A. The multi-jet background is estimated using a data-driven method, while the diboson contribution is normalised to luminosity. The yellow band shows only the combined JES, JER and MC statistics uncertainties. Other correlated systematic uncertainties, such as those due to theoretical modelling, are not shown. Two mSUGRA/CMSSM benchmark model points with m_0=500 GeV, $m_{1/2}$=570 GeV, A_0=0, $\tan\beta$=10 and $\mu > 0$ and with m_0=2500 GeV, $m_{1/2}$=270 GeV, A_0=0, $\tan\beta$=10 and $\mu > 0$, illustrating different topologies, are also shown. These points lie just beyond the reach of the previous analysis [17]. The red arrow indicates the location of the lower edge of the signal region.

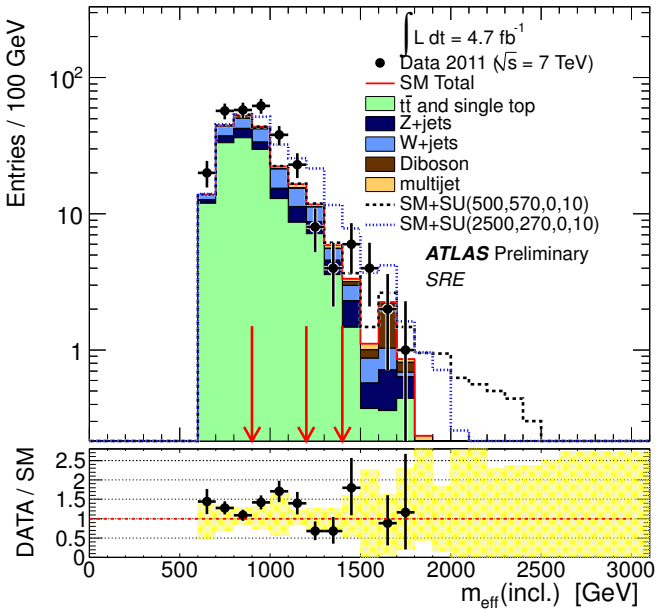

Figure 6: Observed m_{eff}(incl.) distribution for channel E. The histograms show the SM background expectations from MC. The ALPGEN W+jets, Z+jets and $t\bar{t}$ and single top distributions are normalised to data in corresponding control regions for channel A. The multi-jet background is estimated using a data-driven method, while the diboson contribution is normalised to luminosity. The yellow band shows only the combined JES, JER and MC statistics uncertainties. Other correlated systematic uncertainties, such as those due to theoretical modelling, are not shown. Two mSUGRA/CMSSM benchmark model points with m_0=500 GeV, $m_{1/2}$=570 GeV, A_0=0, $\tan\beta$=10 and $\mu > 0$ and with m_0=2500 GeV, $m_{1/2}$=270 GeV, A_0=0, $\tan\beta$=10 and $\mu > 0$, illustrating different topologies, are also shown. These points lie just beyond the reach of the previous analysis [17]. The red arrows indicate the locations of the lower edges of the three signal regions.

Process	Signal Region					
	SRC loose	SRE loose	SRA medium	SRA' medium	SRC medium	SRE medium
$t\bar{t}$+ Single Top	74 ± 13 (75)	66 ± 26 (64)	7 ± 5 (5.1)	11 ± 3.4 (10)	12 ± 4.5 (10)	17 ± 5.8 (13)
Z/γ+jets	70 ± 22 (61)	22 ± 6.4 (13)	31 ± 9.9 (34)	64 ± 20 (69)	17 ± 5.9 (16)	8 ± 2.9 (4.4)
W+jets	62 ± 9.3 (61)	23 ± 11 (23)	19 ± 4.5 (21)	26 ± 4.6 (30)	8.1 ± 2.9 (11)	5.9 ± 3 (4.7)
Multi-jets	0.39 ± 0.4 (0.16)	3.7 ± 1.9 (3.8)	0.14 ± 0.24 (0.13)	0 ± 0.13 (0.38)	0.024 ± 0.034 (0.013)	0.8 ± 0.53 (0.64)
Di-Bosons	7.9 ± 4 (7.9)	4.2 ± 2 (4.2)	7.3 ± 3.7 (7.5)	15 ± 7.4 (16)	1.7 ± 0.87 (1.7)	2.7 ± 1.3 (2.7)
Total	214 ± 24.9 ± 13	119 ± 32.6 ± 11.6	64.8 ± 10.2 ± 6.92	115 ± 19 ± 9.69	38.6 ± 6.68 ± 4.77	34 ± 4.47 ± 5.57
Data	210	148	59	85	36	25
local p-value (Gaus. σ)	0.55(-0.14)	0.21(0.8)	0.65(-0.4)	0.9(-1.3)	0.6(-0.26)	0.85(-1)
UL on N_{BSM}	$58(60^{44}_{83})$	$84(69^{52}_{93})$	$25(28^{20}_{39})$	$29(43^{32}_{60})$	$18(19^{14}_{27})$	$12(16^{12}_{23})$
UL on σ_{BSM} /(fb)	$12(13^{9.3}_{18})$	$18(15^{11}_{20})$	$5.3(6^{4.3}_{8.2})$	$6.2(9.2^{6.7}_{13})$	$3.7(4.1^{3}_{5.7})$	$2.5(3.5^{2.5}_{5})$

Process	Signal Region				
	SRA tight	SRB tight	SRC tight	SRD tight	SRE tight
$t\bar{t}$+ Single Top	0.22 ± 0.35 (0.046)	0.21 ± 0.33 (0.066)	1.8 ± 1.6 (0.96)	2 ± 1.7 (0.92)	3.9 ± 4 (2.6)
Z/γ+jets	2.9 ± 1.5 (3.1)	2.5 ± 1.4 (1.6)	2.1 ± 1.1 (4.4)	0.95 ± 0.58 (2.7)	3.2 ± 1.4 (1.8)
W+jets	2.1 ± 0.99 (1.9)	0.97 ± 0.6 (0.84)	1.2 ± 1.2 (2.7)	1.7 ± 1.5 (2.5)	2.3 ± 1.7 (1.5)
Multi-jets	0 ± 0.0024 (0.002)	0 ± 0.0034 (0.0032)	0 ± 0.0058 (0.0023)	0 ± 0.0072 (0.021)	0.22 ± 0.25 (0.24)
Di-Bosons	1.7 ± 0.95 (2)	1.7 ± 0.95 (1.9)	0.49 ± 0.26 (0.51)	2.2 ± 1.2 (2.2)	2.5 ± 1.3 (2.5)
Total	7 ± 0.999 ± 2.26	5.39 ± 0.951 ± 2.01	5.68 ± 1.79 ± 1.51	6.84 ± 1.7 ± 2.1	12.1 ± 4.59 ± 3.04
Data	1	1	14	9	13
local p-value (Gaus. σ)	0.98(-2.1)	0.95(-1.7)	0.018(2.1)	0.29(0.55)	0.45(0.13)
UL on N_{BSM}	$2.9(6.1^{4.2}_{9})$	$3.1(5.5^{3.8}_{8.3})$	$16(11^{7.6}_{15})$	$10(8.9^{6.4}_{13})$	$12(12^{8.5}_{17})$
UL on σ_{BSM} /(fb)	$0.62(1.3^{0.89}_{1.9})$	$0.65(1.2^{0.8}_{1.8})$	$3.5(2.3^{1.6}_{3.2})$	$2.2(1.9^{1.4}_{2.7})$	$2.6(2.5^{1.8}_{3.5})$

Table 3: Observed numbers of events in data and fitted background components in each SR. For the total background estimates, the quoted errors give the systematic and statistical (MC and CR combined) uncertainties respectively. For the individual background components, the total uncertainties are given, with the values in parenthesis indicating the pre-fit predictions for the MC expectations. For W+jets, Z+jets and $t\bar{t}$+jets, these predictions are from ALPGEN, and scaled by additional factors of 0.75, 0.78 and 0.73 respectively, determined by normalisation to data in corresponding control regions in channel A. In the case of the multi-jet background, the pre-fit values are from the data-driven method. The p-values give the probability of the observation being consistent with the estimated background, and the "Gaus. σ" values the number of standard deviations in a Gaussian approximation, evaluated for a single observation at a time. The last two lines show the upper limits on the excess number of events, and the excess cross-section, above that expected from the Standard Model. The observed upper limit is followed in brackets by the expected limit, with the super- and sub-scripts showing the variation in the expectation from $\pm 1\sigma$ changes in the background.

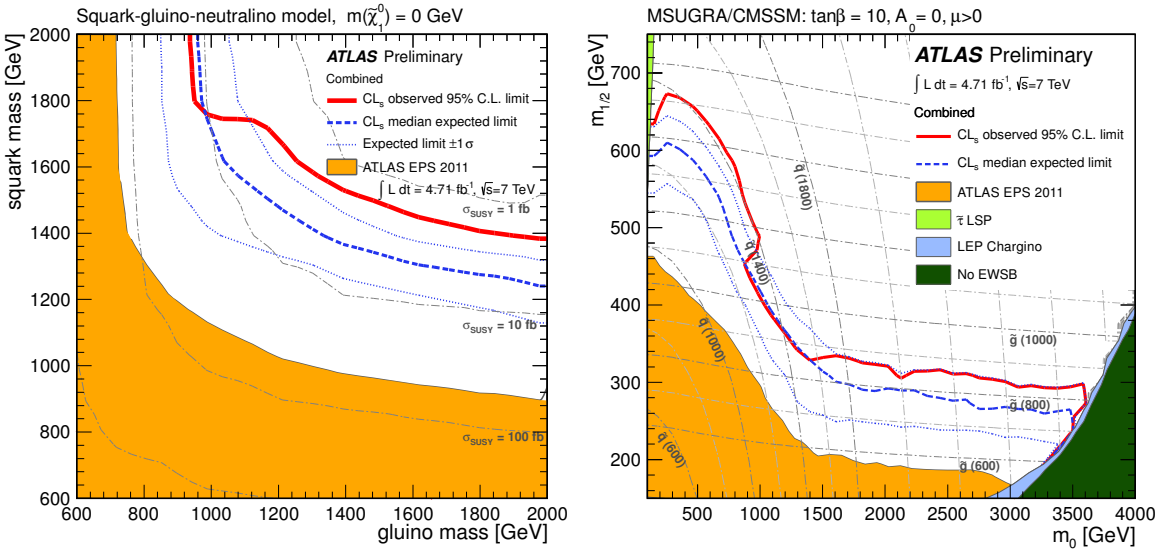

Figure 7: 95% CL_s exclusion limits obtained by using the signal region with the best expected sensitivity at each point in a simplified MSSM scenario with only strong production of gluinos and first- and second-generation squarks, and direct decays to jets and neutralinos (left); and in the (m_0 ; $m_{1/2}$) plane of MSUGRA/CMSSM for $\tan\beta = 10$, $A_0 = 0$ and $\mu > 0$ (right). The red lines show the observed limits, the dashed-blue lines the median expected limits, and the dotted blue lines the $\pm 1\sigma$ variation on the expected limits. ATLAS EPS 2011 limits are from [17] and LEP results from [59].

7 Summary

This note reports a search for new physics in final states containing high-p_{T} jets, missing transverse momentum and no electrons or muons, based on the full dataset (4.7 fb^{-1}) recorded by the ATLAS experiment at the LHC in 2011. Good agreement is seen between the numbers of events observed in the data and the numbers of events expected from SM processes.

The results are interpreted in both a simplified model containing only squarks of the first two generations, a gluino octet and a massless neutralino, as well as in MSUGRA/CMSSM models with $\tan\beta = 10$, $A_0 = 0$ and $\mu > 0$. In the simplified model, gluino masses below 940 GeV and squark masses below 1380 GeV are excluded at the 95% confidence level. In the MSUGRA/CMSSM models, values of $m_{1/2} < 300$ GeV are excluded for all values of m_0, and $m_{1/2} < 680$ GeV for low m_0. Equal mass squarks and gluinos are excluded below 1400 GeV in both scenarios.

References

[1] L. Evans and P. Bryant, *LHC Machine*, JINST **3** (2008) S08001.

[2] H. Miyazawa, *Baryon Number Changing Currents*, Prog. Theor. Phys. **36 (6)** (1966) 1266–1276.

[3] P. Ramond, *Dual Theory for Free Fermions*, Phys. Rev. **D3** (1971) 2415–2418.

[4] Y. A. Golfand and E. P. Likhtman, *Extension of the Algebra of Poincare Group Generators and Violation of p Invariance*, JETP Lett. **13** (1971) 323–326. [Pisma Zh.Eksp.Teor.Fiz.13:452-455,1971].

[5] A. Neveu and J. H. Schwarz, *Factorizable dual model of pions*, Nucl. Phys. **B31** (1971) 86–112.

[6] A. Neveu and J. H. Schwarz, *Quark Model of Dual Pions*, Phys. Rev. **D4** (1971) 1109–1111.

[7] J. Gervais and B. Sakita, *Field theory interpretation of supergauges in dual models*, Nucl. Phys. **B34** (1971) 632–639.

[8] D. V. Volkov and V. P. Akulov, *Is the Neutrino a Goldstone Particle?*, Phys. Lett. **B46** (1973) 109–110.

[9] J. Wess and B. Zumino, *A Lagrangian Model Invariant Under Supergauge Transformations*, Phys. Lett. **B49** (1974) 52.

[10] J. Wess and B. Zumino, *Supergauge Transformations in Four-Dimensions*, Nucl. Phys. **B70** (1974) 39–50.

[11] P. Fayet, *Supersymmetry and Weak, Electromagnetic and Strong Interactions*, Phys. Lett. **B64** (1976) 159.

[12] P. Fayet, *Spontaneously Broken Supersymmetric Theories of Weak, Electromagnetic and Strong Interactions*, Phys. Lett. **B69** (1977) 489.

[13] G. R. Farrar and P. Fayet, *Phenomenology of the Production, Decay, and Detection of New Hadronic States Associated with Supersymmetry*, Phys. Lett. **B76** (1978) 575–579.

[14] P. Fayet, *Relations Between the Masses of the Superpartners of Leptons and Quarks, the Goldstino Couplings and the Neutral Currents*, Phys. Lett. **B84** (1979) 416.

[15] S. Dimopoulos and H. Georgi, *Softly Broken Supersymmetry and SU(5)*, Nucl. Phys. **B193** (1981) 150.

[16] ATLAS Collaboration, *Search for supersymmetry in final states with jets, missing transverse momentum and one isolated lepton in* $\sqrt{s} = 7$ *TeV pp collisions using 1* fb^{-1} *of ATLAS data*, Phys.Rev. **D85** (2012) 012006, arXiv:1109.6606 [hep-ex].

[17] ATLAS Collaboration, J. B. G. da Costa et al., *Search for squarks and gluinos using final states with jets and missing transverse momentum with the ATLAS detector in* $\sqrt{s} = 7$ *TeV proton-proton collisions*, arXiv:1102.5290 [hep-ex].

[18] ATLAS Collaboration, *The ATLAS Experiment at the CERN Large Hadron Collider*, 2008. JINST **3** (2008) S08003.

[19] M. Cacciari, G. P. Salam, and G. Soyez, *The anti-k_t jet clustering algorithm*, JHEP **04** (2008) 063, arXiv:0802.1189 [hep-ph].

[20] M. Cacciari and G. P. Salam, *Dispelling the N^3 myth for the k_t jet-finder*, Phys. Lett. **B641** (2006) 57–61, arXiv:hep-ph/0512210.

[21] W. Lampl et al., *Calorimeter Clustering Algorithms: Description and Performance*, Tech. Rep. ATL-LARG-PUB-2008-002, CERN, 2011 .

[22] ATLAS Collaboration, *Jet energy scale and its systematic uncertainty in proton-proton collisions at* $\sqrt{s} = 7$ *TeV in ATLAS 2010 data*, 2010. ATLAS-CONF-2011-032.

[23] ATLAS Collaboration, *Electron performance measurements with the ATLAS detector using the 2010 LHC proton-proton collision data*, arXiv:1110.3174 [hep-ex].

[24] ATLAS Collaboration, *Expected Performance of the ATLAS Experiment - Detector, Trigger and Physics*, CERN-OPEN-2008-020. arXiv:0901.0512 [hep-ex].

[25] ATLAS Collaboration, *Jet energy measurement with the ATLAS detector in proton-proton collisions at* $\sqrt{s}$ *= 7 TeV*, arXiv:1112.6426 [hep-ex]. Submitted to Eur. Phys. J. C.

[26] ATLAS Collaboration, G. Aad et al., *Search for squarks and gluinos using final states with jets and missing transverse momentum with the ATLAS detector in* $\sqrt{s}$ *= 7 TeV proton-proton collisions*, arXiv:1109.6572 [hep-ex]. Accepted by Phys. Lett. B.

[27] T. Sjostrand, S. Mrenna, and P. Z. Skands, *PYTHIA 6.4 Physics and Manual*, JHEP **0605** (2006) 026, arXiv:hep-ph/0603175.

[28] A. Sherstnev and R. S. Thorne, *Parton Distributions for LO Generators*, Eur. Phys. J. **C55** (2008) 553–575, arXiv:0711.2473 [hep-ph].

[29] M. L. Mangano, M. Moretti, F. Piccinini, R. Pittau, and A. D. Polosa, *ALPGEN, a generator for hard multiparton processes in hadronic collisions*, JHEP **07** (2003) 001, arXiv:hep-ph/0206293.

[30] J. Pumplin, D. Stump, J. Huston, H. Lai, P. M. Nadolsky, et al., *New generation of parton distributions with uncertainties from global QCD analysis*, JHEP **0207** (2002) 012, arXiv:hep-ph/0201195 [hep-ph].

[31] T. Gleisberg et al., *Event generation with SHERPA 1.1*, JHEP **0902** (2009) 007, arXiv:0811.4622 [hep-ph].

[32] S. Frixione, E. Laenen, P. Motylinski, and B. R. Webber, *Single-top production in MC@NLO*, JHEP **03** (2006) 092, arXiv:hep-ph/0512250.

[33] S. Frixione, E. Laenen, P. Motylinski, B. R. Webber, and C. D. White, *Single-top hadroproduction in association with a W boson*, JHEP **07** (2008) 029, arXiv:0805.3067 [hep-ph].

[34] P. M. Nadolsky et al., *Implications of CTEQ global analysis for collider observables*, Phys. Rev. **D78** (2008) 013004.

[35] G. Corcella et al., *HERWIG 6.5: an event generator for Hadron Emission Reactions With Interfering Gluons (including supersymmetric processes)*, JHEP **01** (2001) 010, arXiv:hep-ph/0011363.

[36] G. Corcella et al., *HERWIG 6.5 release note*, 2002. arXiv:hep-ph/0210213.

[37] J. M. Butterworth, J. R. Forshaw, and M. H. Seymour, *Multiparton interactions in photoproduction at HERA*, Z. Phys. **C72** (1996) 637–646, arXiv:hep-ph/9601371.

[38] M. Bahr et al., *Herwig++ Physics and Manual*, Eur. Phys. J. **C58** (2008) 639–707, arXiv:0803.0883 [hep-ph].

[39] W. Beenakker, R. Hopker, M. Spira, and P. M. Zerwas, *Squark and gluino production at hadron colliders*, Nucl. Phys. **B492** (1997) 51–103, arXiv:hep-ph/9610490.

[40] A. Kulesza and L. Motyka, *Threshold resummation for squark-antisquark and gluino-pair production at the LHC*, Phys.Rev.Lett. **102** (2009) 111802, arXiv:0807.2405 [hep-ph].

[41] A. Kulesza and L. Motyka, *Soft gluon resummation for the production of gluino-gluino and squark-antisquark pairs at the LHC*, Phys.Rev. **D80** (2009) 095004, arXiv:0905.4749 [hep-ph].

[42] W. Beenakker et al., *Soft-gluon resummation for squark and gluino hadroproduction*, JHEP **0912** (2009) 041, arXiv:0909.4418 [hep-ph].

[43] W. Beenakker, S. Brensing, M. Kramer, A. Kulesza, E. Laenen, et al., *Squark and gluino hadroproduction*, Int.J.Mod.Phys. **A26** (2011) 2637–2664, arXiv:1105.1110 [hep-ph].

[44] M. Botje et al., *The PDF4LHC Working Group Interim Recommendations*, arXiv:1101.0538 [hep-ph].

[45] A. Martin, W. Stirling, R. Thorne, and G. Watt, *Parton distributions for the LHC*, Eur.Phys.J. **C63** (2009) 189–285, arXiv:0901.0002 [hep-ph].

[46] The ATLAS Collaboration, *ATLAS tunes of PYTHIA 6 and Pythia 8 for MC11*, ATLAS Note (2011) ATL-PHYS-PUB-2011-009.

[47] The ATLAS Collaboration, *Further ATLAS tunes of PYTHIA6 and Pythia 8*, ATLAS Note (2011) ATL-PHYS-PUB-2011-014.

[48] The ATLAS Collaboration, *First tuning of HERWIG/JIMMY to ATLAS data*, ATLAS Note (2010) ATL-PHYS-PUB-2010-014.

[49] GEANT4 Collaboration, S. Agostinelli et al., *GEANT4: A simulation toolkit*, Nucl. Instrum. Meth. **A506** (2003) 250–303.

[50] ATLAS Collaboration, *The ATLAS Simulation Infrastructure*, Eur. Phys. J. **C70** (2010) 823–874, arXiv:1005.4568 [physics.ins-det].

[51] A. Read, *Presentation of search results: the CLs technique*, Journal of Physics G: Nucl. Part. Phys. **28** (2002) 2693–2704.

[52] F. E. Paige, S. D. Protopopescu, H. Baer, and X. Tata, *ISAJET 7.69: A Monte Carlo event generator for p p, anti-p p, and e+ e- reactions*, arXiv:hep-ph/0312045.

[53] A. H. Chamseddine, R. L. Arnowitt, and P. Nath, *Locally Supersymmetric Grand Unification*, Phys.Rev.Lett. **49** (1982) 970.

[54] R. Barbieri, S. Ferrara, and C. A. Savoy, *Gauge Models with Spontaneously Broken Local Supersymmetry*, Phys. Lett. **B119** (1982) 343.

[55] L. E. Ibanez, *Locally Supersymmetric SU(5) Grand Unification*, Phys.Lett. **B118** (1982) 73.

[56] L. J. Hall, J. D. Lykken, and S. Weinberg, *Supergravity as the Messenger of Supersymmetry Breaking*, Phys.Rev. **D27** (1983) 2359–2378.

[57] N. Ohta, *Grand unified theories based on local supersymmetry*, Prog.Theor.Phys. **70** (1983) 542.

[58] G. L. Kane, C. F. Kolda, L. Roszkowski, and J. D. Wells, *Study of constrained minimal supersymmetry*, Phys.Rev. **D49** (1994) 6173–6210, arXiv:hep-ph/9312272 [hep-ph].

[59] DELPHI Collaboration, J. Abdallah et al., *Searches for supersymmetric particles in e^+e^- collisions up to 208 GeV and interpretation of the results within the MSSM.*, Eur. Phys. J. C **31** (Nov, 2003) 421–479. 103 p.

A Supplementary m_{eff} plots for control regions used in the analysis

The ALPGEN W+jets, Z+jets and $t\bar{t}$ and single top distributions in all cases are scaled by factors of respectively 0.75, 0.78 and 0.73 with respect to the raw normalisation by NLO cross-section times luminosity, in order to improve the agreement with the data. These scaling factors are within the expected range of the systematic uncertainties and are determined by normalisation to all data (i.e. without any m_{eff} cut) in CR3, CR1b and CR4 respectively in channel A (i.e. two-jet events). The CR1a plots use ALPGEN without any NLO k-factor or other scaling. The multi-jet background is estimated using a data-driven jet smearing method, while the diboson contribution is normalised to luminosity.

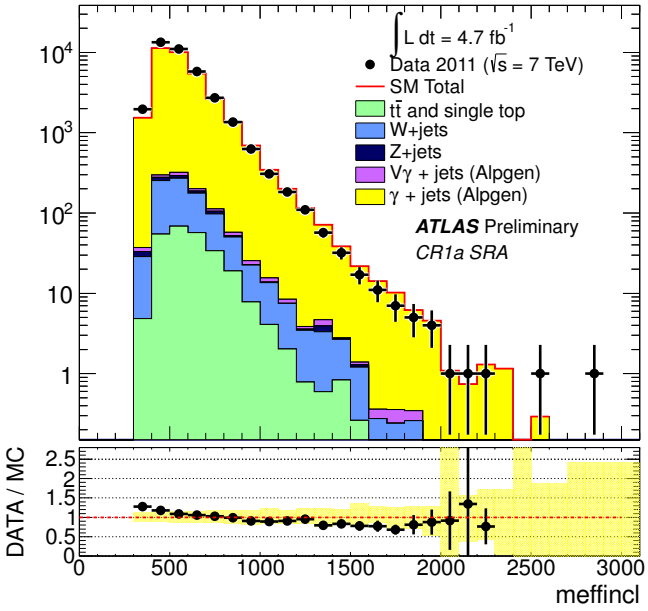

Figure 8: Observed CR1a m_{eff}(incl.) distributions for channel A. The histogram shows the expectation from ALPGEN MC normalised as described above. The yellow band shows only the combined JES, JER and MC statistics uncertainties.

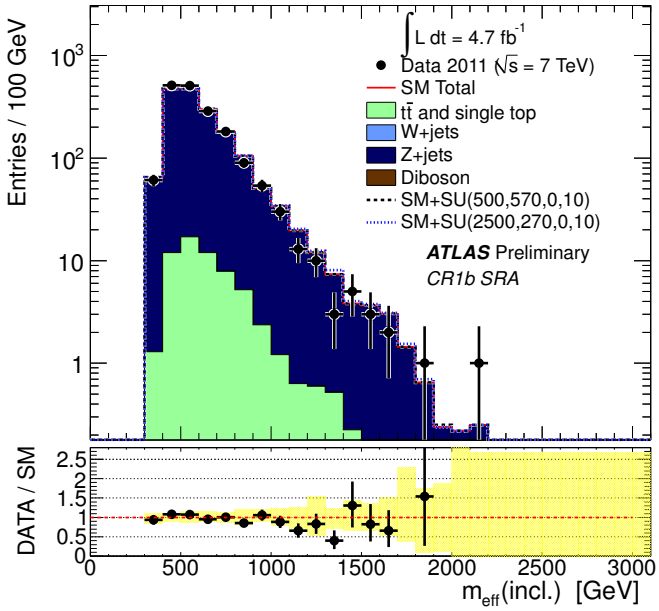

Figure 9: Observed CR1b m_{eff}(incl.) distribution for channel A. The histograms show the normalised SM background expectations. The yellow band shows only the combined JES, JER and MC statistics uncertainties.

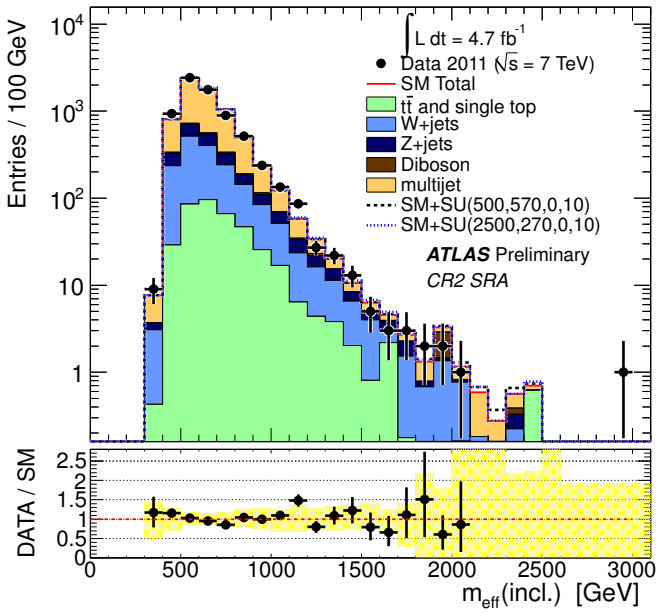

Figure 10: Observed CR2 m_{eff}(incl.) distribution for channel A. Histograms are as for Figure 9.

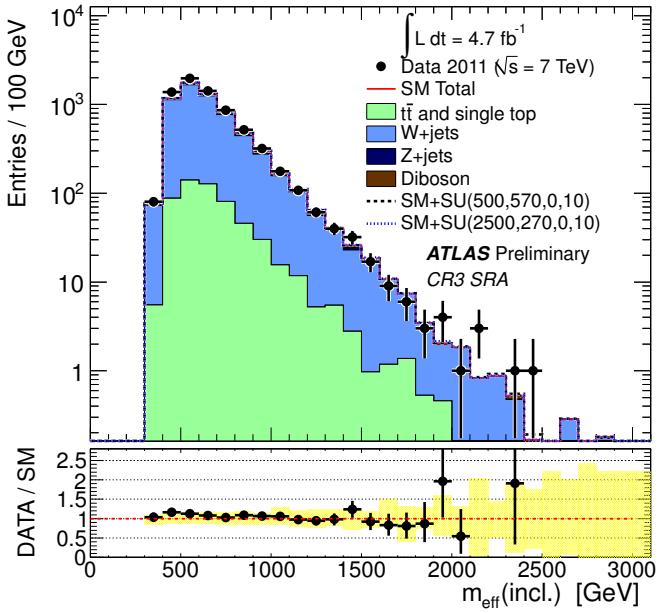

Figure 11: Observed CR3 m_{eff}(incl.) distribution for channel A. Histograms are as for Figure 9.

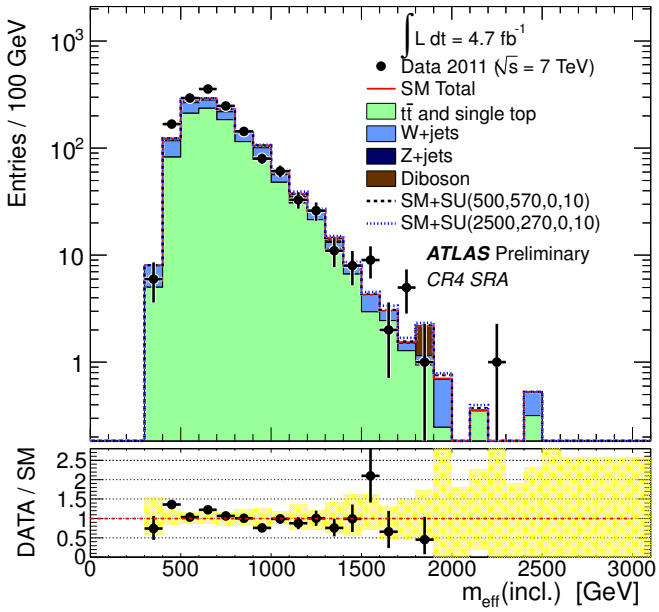

Figure 12: Observed CR4 m_{eff}(incl.) distribution for channel A. Histograms are as for Figure 9.

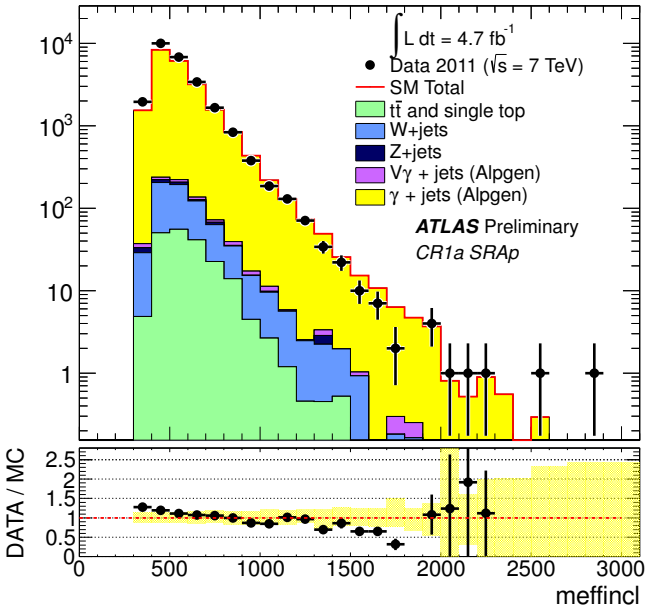

Figure 13: Observed CR1a m_{eff}(incl.) distribution for channel A'. Histograms are as for Figure 8.

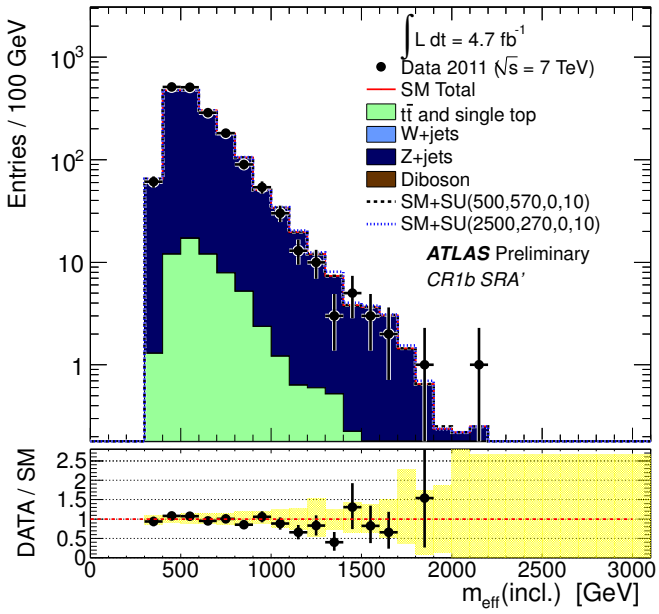

Figure 14: Observed CR1b m_{eff}(incl.) distribution for channel A'. Histograms are as for Figure 9.

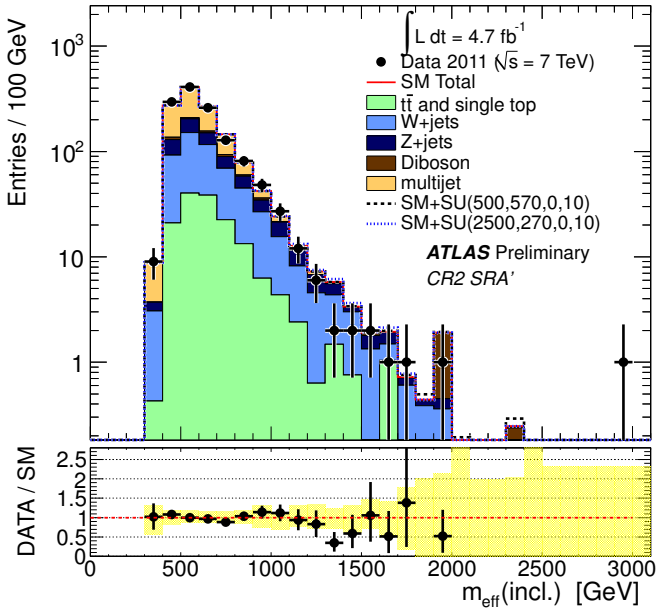

Figure 15: Observed CR2 m_{eff}(incl.) distribution for channel A'. Histograms are as for Figure 9.

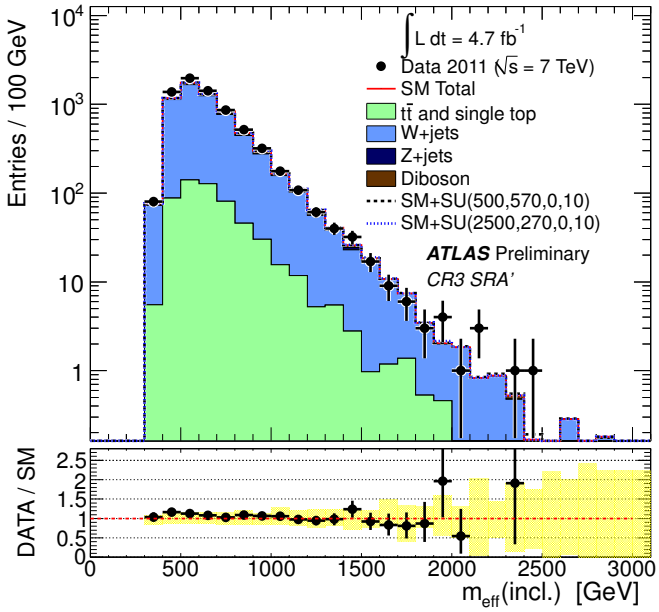

Figure 16: Observed CR3 m_{eff}(incl.) distribution for channel A'. Histograms are as for Figure 9.

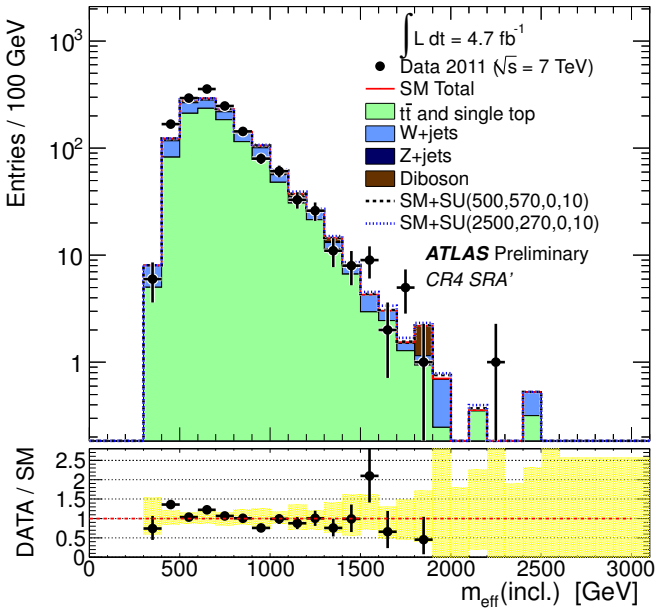

Figure 17: Observed CR4 m_{eff}(incl.) distribution for channel A'. Histograms are as for Figure 9.

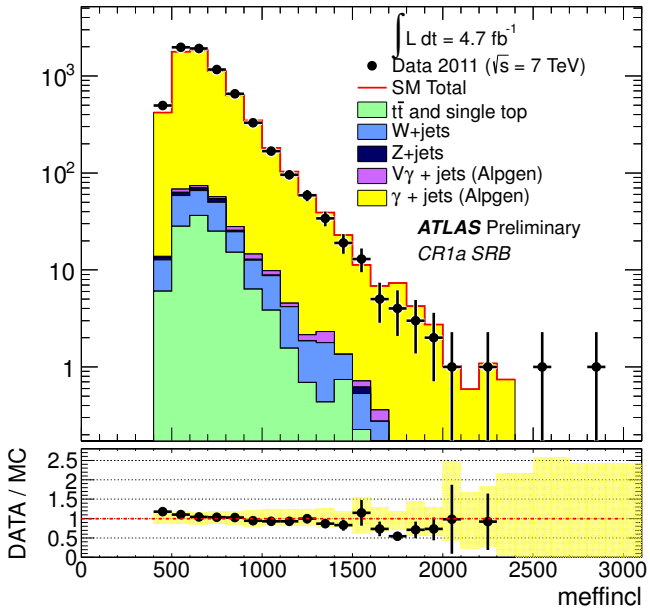

Figure 18: Observed CR1a m_{eff}(incl.) distribution for channel B. Histograms are as for Figure 8.

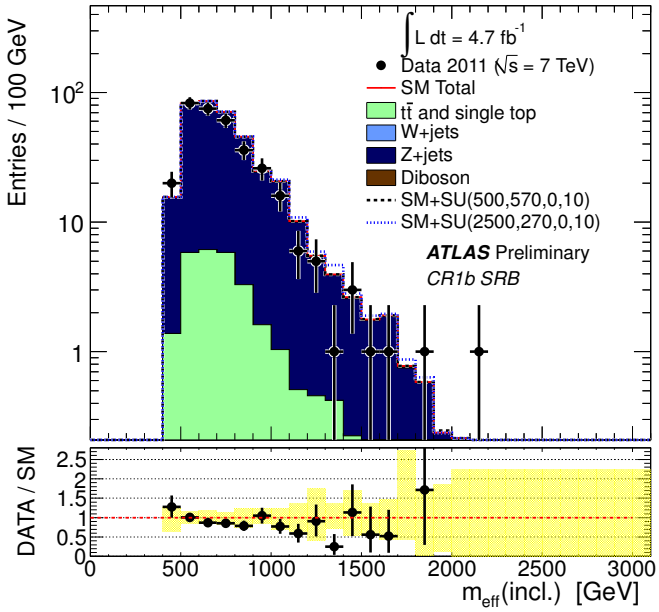

Figure 19: Observed CR1b m_{eff}(incl.) distribution for channel B. Histograms are as for Figure 9.

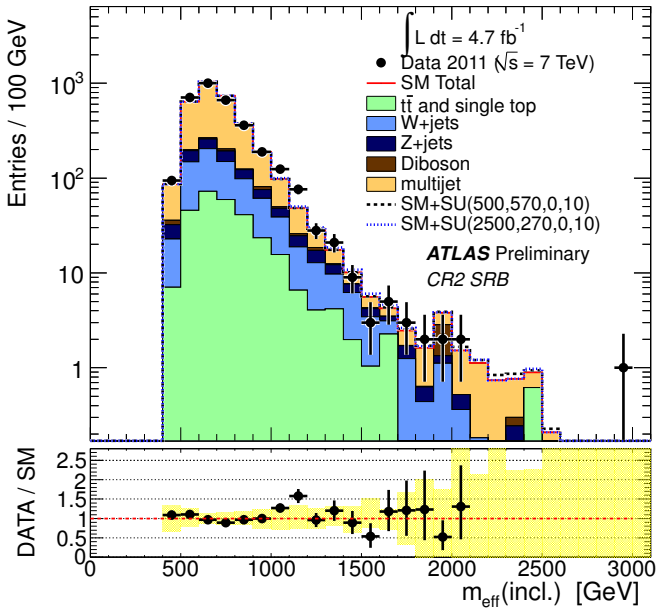

Figure 20: Observed CR2 m_{eff}(incl.) distribution for channel B. Histograms are as for Figure 9.

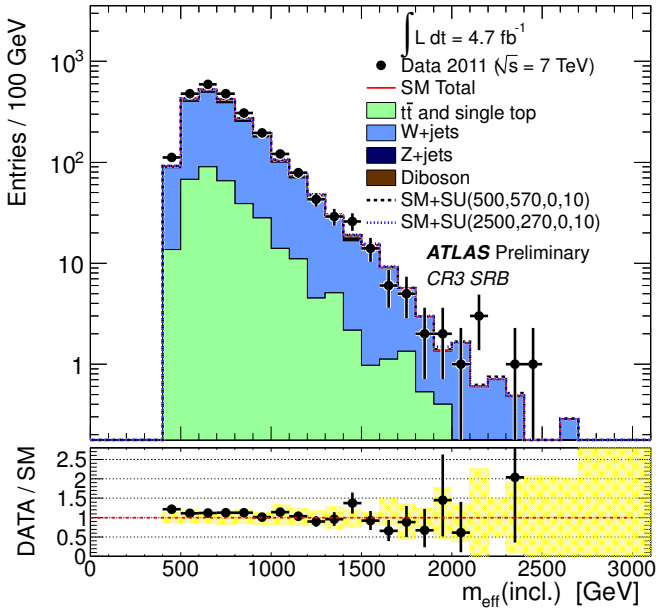

Figure 21: Observed CR3 m_{eff}(incl.) distribution for channel B. Histograms are as for Figure 9.

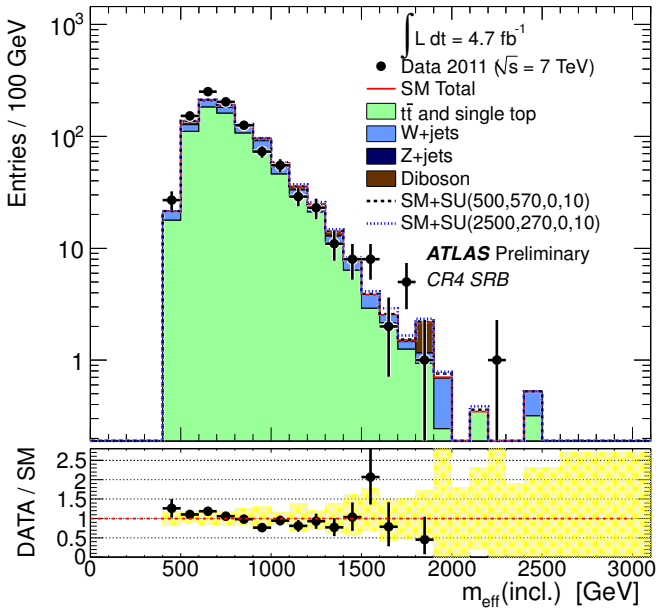

Figure 22: Observed CR4 m_{eff}(incl.) distribution for channel B. Histograms are as for Figure 9.

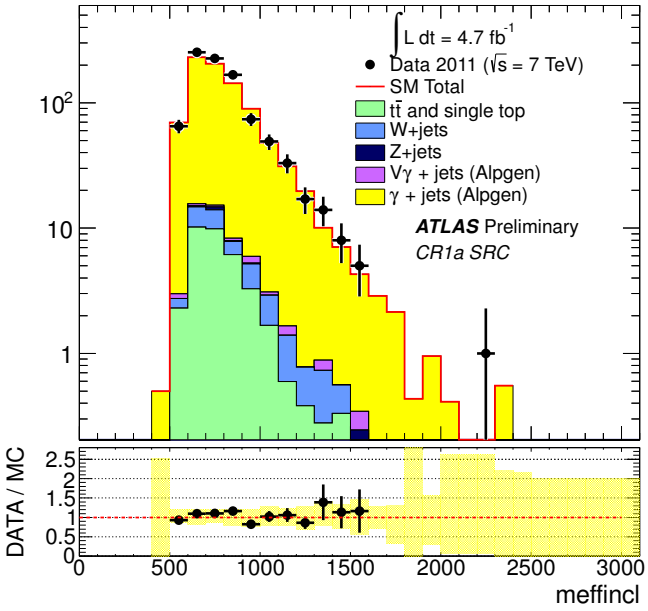

Figure 23: Observed CR1a m_{eff}(incl.) distribution for channel C. Histograms are as for Figure 8.

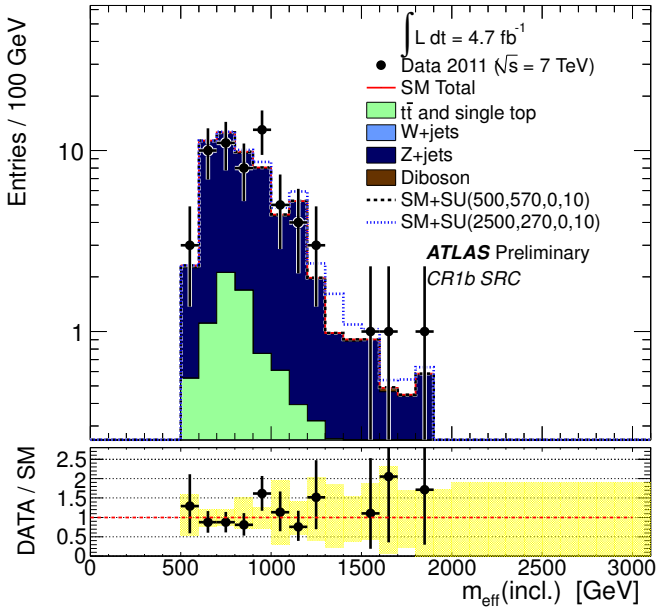

Figure 24: Observed CR1b m_{eff}(incl.) distribution for channel C. Histograms are as for Figure 9.

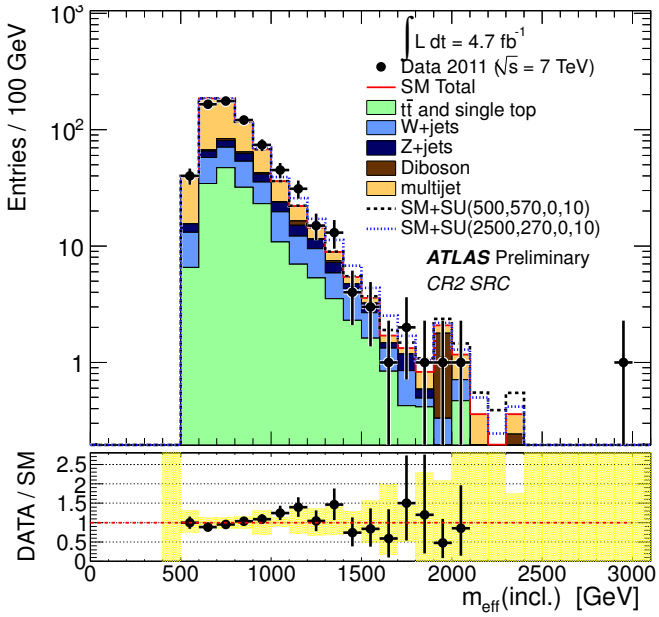

Figure 25: Observed CR2 m_{eff}(incl.) distribution for channel C. Histograms are as for Figure 9.

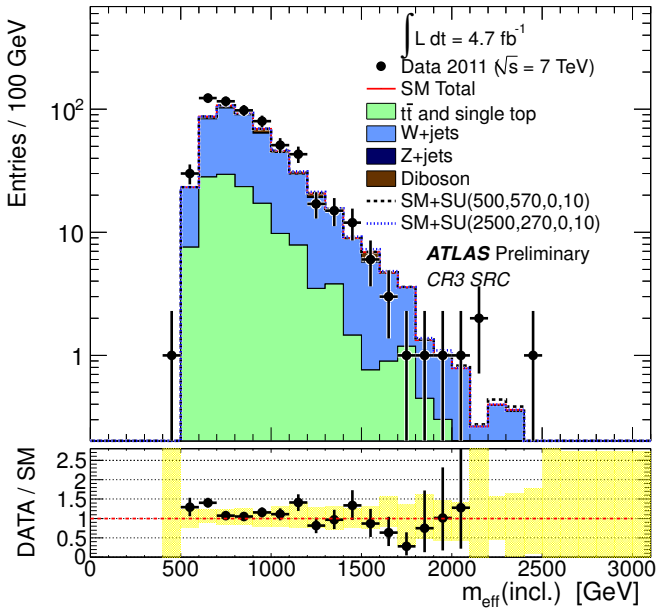

Figure 26: Observed CR3 m_{eff}(incl.) distribution for channel C. Histograms are as for Figure 9.

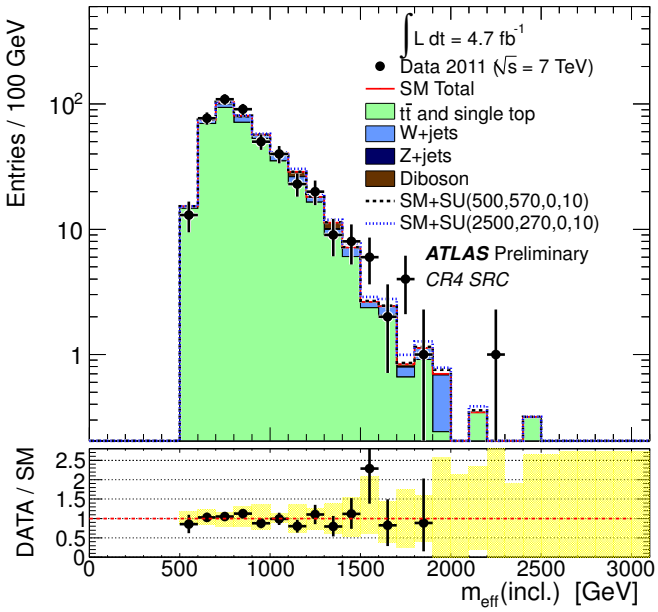

Figure 27: Observed CR4 m_{eff}(incl.) distribution for channel C. Histograms are as for Figure 9.

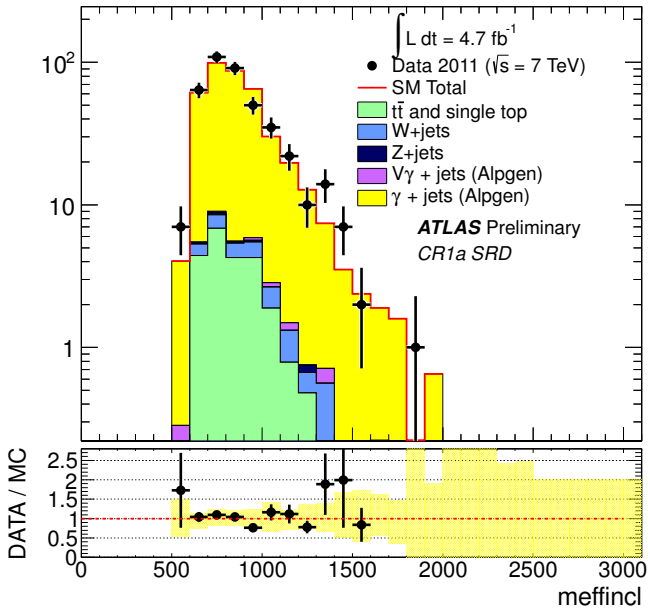

Figure 28: Observed CR1a m_{eff}(incl.) distribution for channel D. Histograms are as for Figure 8.

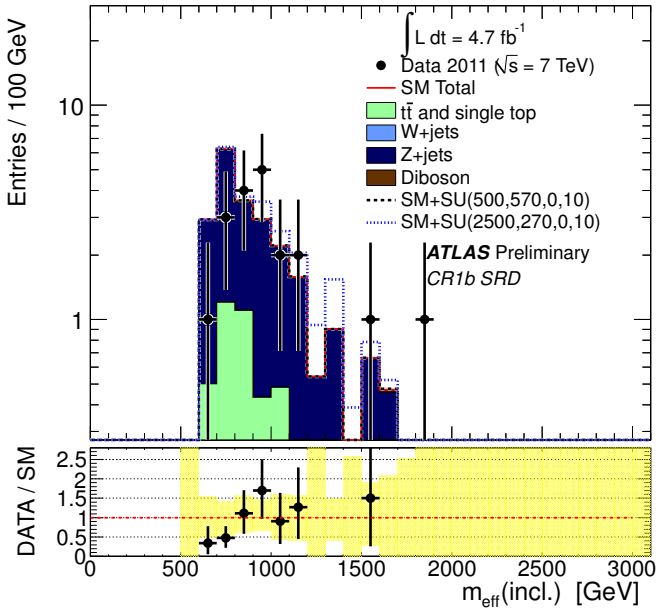

Figure 29: Observed CR1b m_{eff}(incl.) distribution for channel D. Histograms are as for Figure 9.

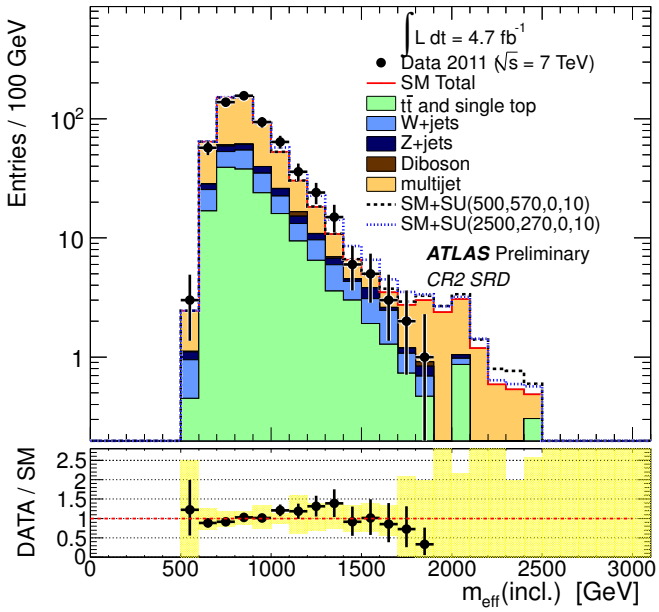

Figure 30: Observed CR2 m_{eff}(incl.) distribution for channel D. Histograms are as for Figure 9.

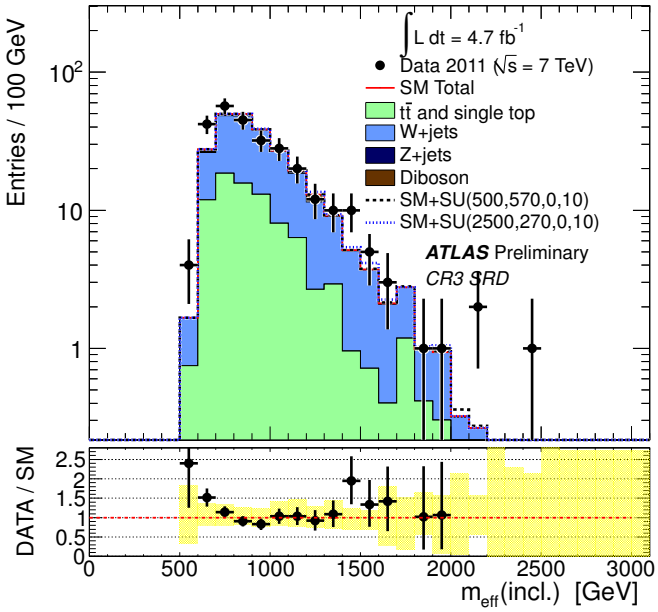

Figure 31: Observed CR3 m_{eff}(incl.) distribution for channel D. Histograms are as for Figure 9.

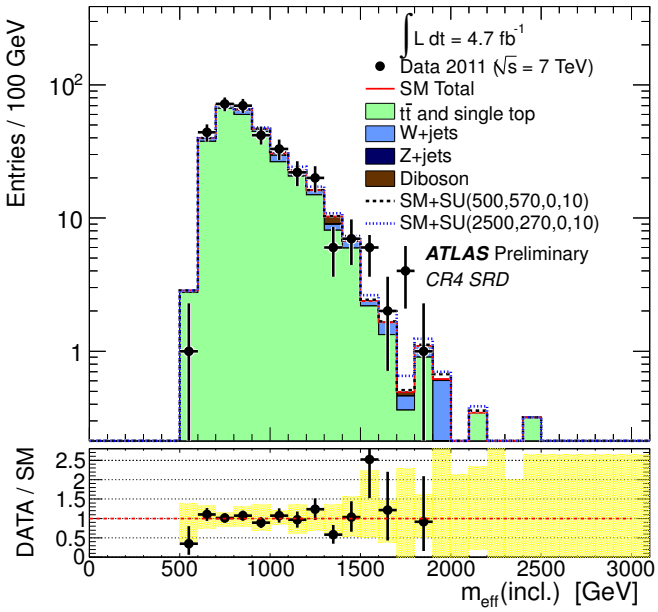

Figure 32: Observed CR4 m_{eff}(incl.) distribution for channel D. Histograms are as for Figure 9.

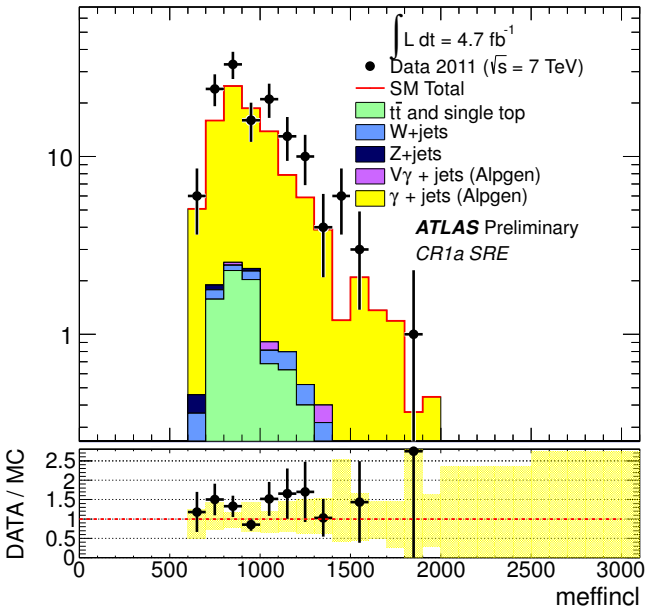

Figure 33: Observed CR1a m_{eff}(incl.) distribution for channel E. Histograms are as for Figure 8.

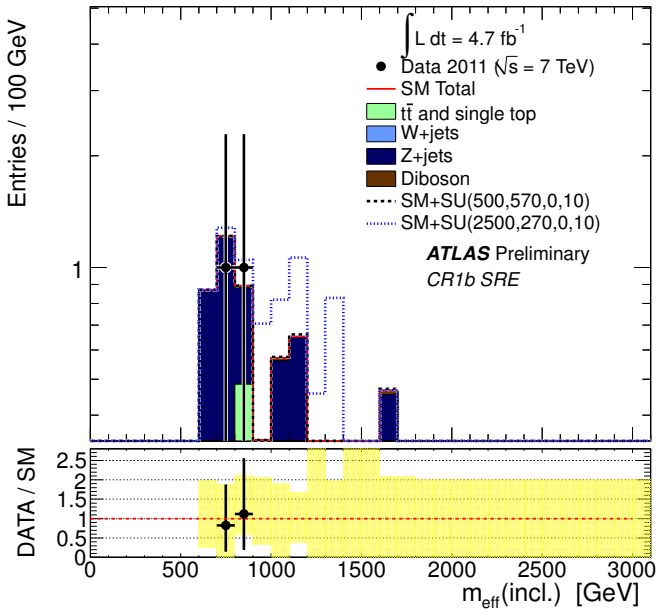

Figure 34: Observed CR1b m_{eff}(incl.) distribution for channel E. Histograms are as for Figure 9.

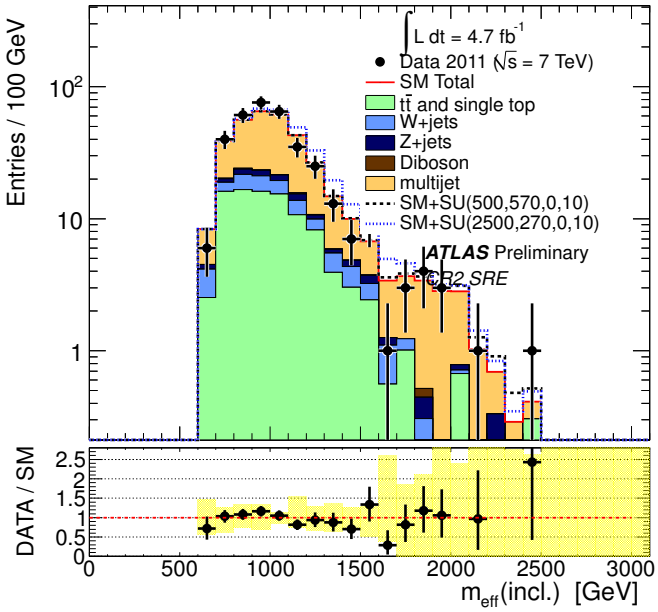

Figure 35: Observed CR2 m_{eff}(incl.) distribution for channel E. Histograms are as for Figure 9.

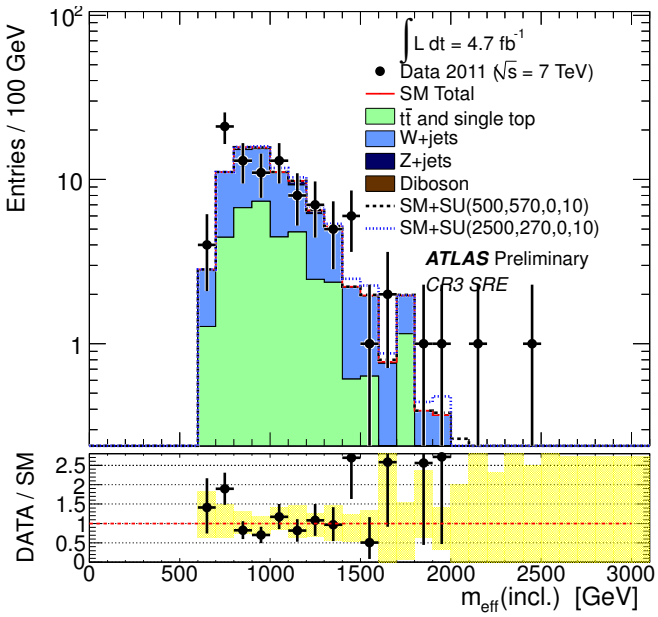

Figure 36: Observed CR3 m_{eff}(incl.) distribution for channel E. Histograms are as for Figure 9.

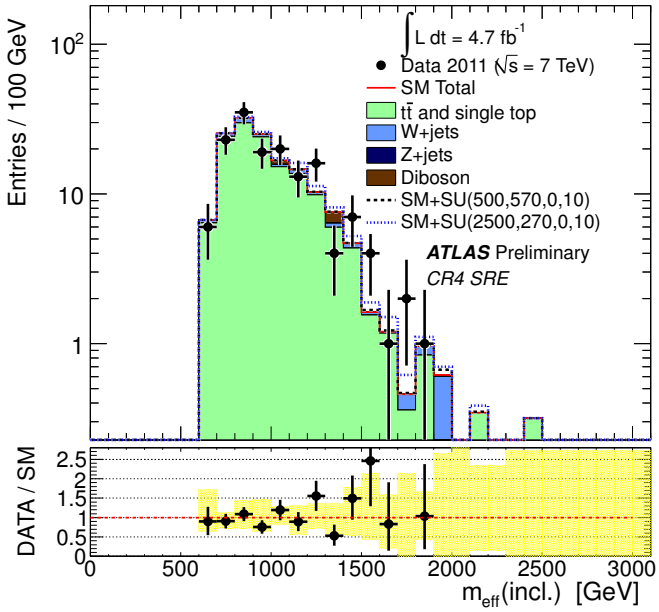

Figure 37: Observed CR4 m_{eff}(incl.) distribution for channel E. Histograms are as for Figure 9.

B Excluded regions in supersymmetry parameter space showing the channel with the best expected exclusion at each point

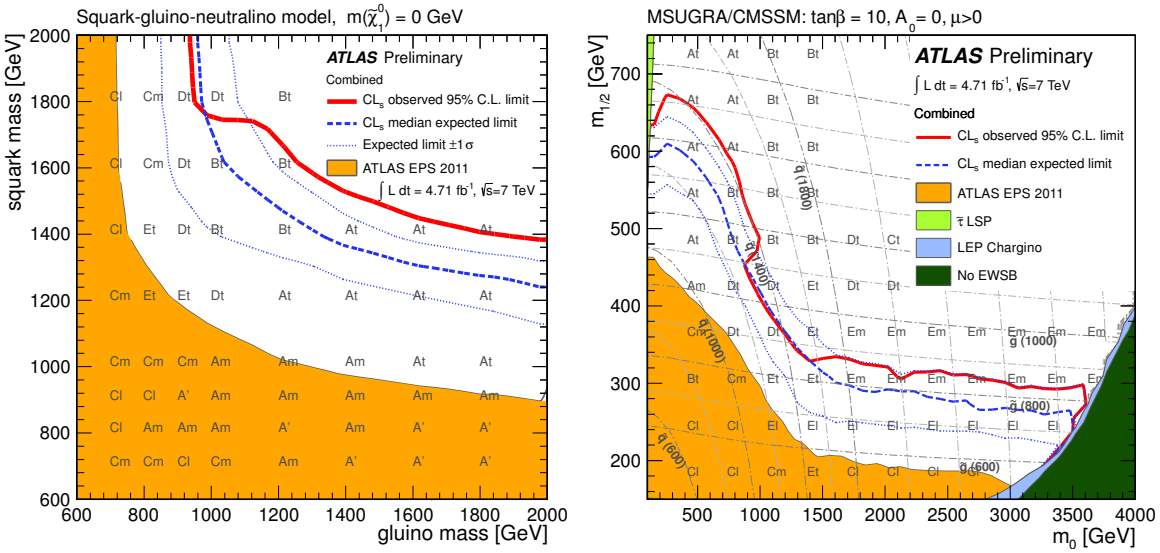

Figure 38: 95% CL_s exclusion limits obtained by using the signal region with the best expected sensitivity at each point in a simplified MSSM scenario with only strong production of gluinos and first- and second-generation squarks, and direct decays to jets and neutralinos (left); and in the (m_0 ; $m_{1/2}$) plane of MSUGRA/CMSSM for $\tan\beta = 10$, $A_0 = 0$ and $\mu > 0$ (right). The red lines show the observed limits, the dashed-blue lines the median expected limits, and the dotted blue lines the $\pm 1\sigma$ variation on the expected limits. The labels A-E refer to the channel with the best expected exclusion at each point, while the suffixes l, m and t refer to the loose, medium and tight selections for each signal region. ATLAS EPS 2011 limits are from [17] and LEP results from [59].

C Event display of the highest m_{eff} event recorded in this data sample.

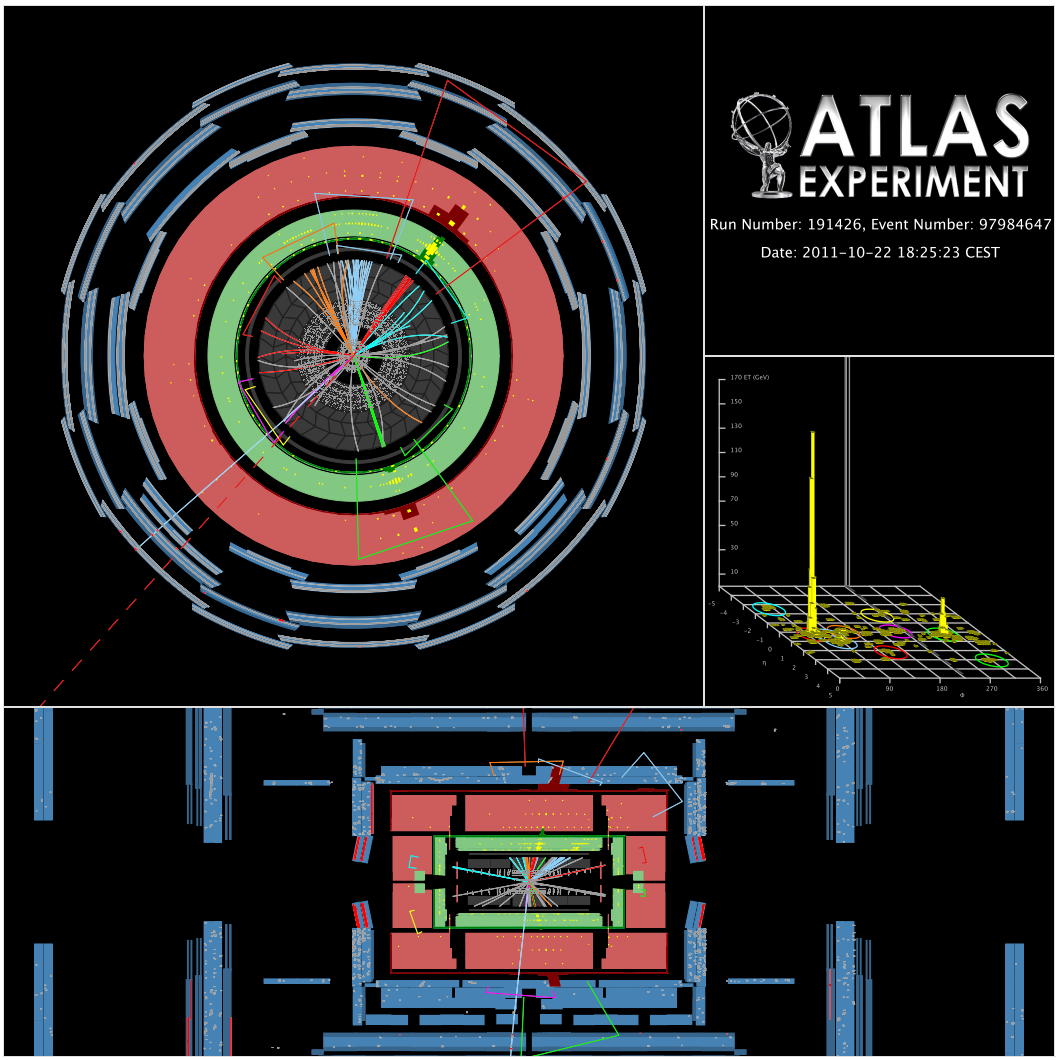

Figure 39: A display of the reconstructed event with the highest m_{eff} found in the data sample used for this note. This event possesses four jets with $p_{\text{T}} > 40$ GeV ($p_{\text{T}} = 974$, 276, 146 and 61 GeV respectively), $E_{\text{T}}^{\text{miss}} = 984$ GeV and $m_{\text{eff}} = 2441$ GeV (calculated using the leading four jets).